Received: 31 January 2019 | Revised: 12 December 2019 | Accepted: 24 January 2020

DOI: 10.1002/nme.6321



RESEARCH ARTICLE

WILEY

# Fluid structure interaction by means of variational multiscale reduced order models

**Alexis Tello**[1] | **Ramon Codina**[1, 2] | **Joan Baiges**[1]

[1]Universitat Politècnica de Catalunya (UPC), Barcelona, Spain

[2]International Centre for Numerical Methods in Engineering (CIMNE), Barcelona, Spain

**Correspondence**
Joan Baiges, Universitat Politécnica de Catalunya (UPC), Jordi Girona 1-3, 08034 Barcelona, Spain.
Email: joan.baiges@upc.edu

**Summary**

A reduced order model designed by means of a variational multiscale stabilized formulation has been applied successfully to fluid-structure interaction problems in a strongly coupled partitioned solution scheme. Details of the formulation and the implementation both for the interaction problem and for the reduced models, for both the off-line and on-line phases, are shown. Results are obtained for cases in which both domains are reduced at the same time. Numerical results are presented for a semistationary and a fully transient case.

**KEYWORDS**

fluid structure Interaction, nonlinear solid elastodynamics, reduced order model, variational multiscale method

## 1 | INTRODUCTION

Fluid structure interaction (FSI) is a topic of constant research and development, and even though fluid and solid formulations might be well understood, FSI remains a complex problem due to factors such as the added mass effect, instabilities of the fluid and solid problems, and the overall conditioning of the problem due to factors like different scales of material parameters (like viscosities of the order of $10^{-3}$ and Young modulus of the order of $10^{6}$, in SI units), temporal stiffness caused by the coupling of a parabolic problem (Navier-Stokes equations) and a hyperbolic one (elasticity equations) and the bad conditioning that arises from the discretization of second-order spatial differential operators.[1] Broadly, research in the field can be grouped into two categories based on how the mesh is treated, namely, conforming and nonconforming methods. Essentially, conforming mesh methods consider interface conditions as physical boundary conditions, thus treating the interface as part of the solution. In this approach, the mesh reproduces or conforms to the interface; when the interface is moved, it is also necessary to displace the mesh, which carries on all related problems of mesh recalculation and inherent instabilities of the method, be it partitioned or monolithic.[2-8] On the other hand, nonconforming methods treat the interface and boundary as constraints imposed on the governing equations, which makes possible to use meshes that do not reproduce the interface; the main problem in this case is the treatment of the interface conditions and the complexity of the formulation[9,10] for further reading. For a general review of significant (FSI) advances and developments, see Reference 11. Overall, for highly nonlinear problems, arriving at a solution can take a large amount of time, an issue that becomes even more apparent when dealing with problems with a high number of degrees of freedom (DOF). It is well known that reduced order models (ROM) can speed up solution time dramatically, which leads to the idea of introducing them into FSI analysis.

Model order reduction (MOR) was originally developed for the area of system control theory, and its main purpose being reducing its complexity while maintaining the input-output behavior. The resulting mathematical approximation to the original full order problem is precisely known as a ROM. From this, MOR rapidly spread to other fields of research quite successfully. Various ways to achieve model reduction and achieve solution speed up are available.[12-16] Among the

  

various families of ROM, proper orthogonal decomposition (POD) gained considerable attention in the area of numerical analysis, particularly in fluid dynamics, because of its applicability to nonlinear partial differential equations. POD is the foundation of the methods used in this work.

In terms of recent FSI-ROM work, we can refer to Reference 17, where the fluid domain hyperreduction is obtained by means of POD-Greedy algorithms applied to the field of hemodynamics. In Reference 18, the authors propose a POD approach for a monolithic FSI, where the basis for the resulting system is obtained in a monolithic way, both for the Newtonian fluid and the linear elastic solid. The idea of their method is the parametrization of variables by means of empirical interpolations, providing accurate results for a range of data considered in the interpolation charts. In Reference 19, the authors introduce the concept of nonintrusive model reduction to the FSI field, making the calculation of the reduced basis problem independently for the fluid and the solid. In terms of solid domain reduction, in Reference 20, the authors apply a modal analysis by means of model recalibration to the movement of a membrane.

Our approach is different, we consider the reduced system to be variational by nature and use the need of stabilization as a way to project the solution of both the fluid and the solid onto the reduced space. This is not the first time stabilization of the reduced problem is done; however, see for example Reference 21, where the idea of *subgrid scales* for ROM is first explored, 22, where for the first time stabilization through the residual of the reduced space is considered, 23, where the residual of the reduced problem is projected into the reduced space where the solution is sought, taking into account a possible orthogonality of the ROM subscales, and finally 24, where a full variational multiscale (VMS)-ROM method is presented considering dynamic and orthogonal subscales. More recently in Reference 25, the authors propose a similar stabilized formulation in the reduced space, which is similar to the one proposed earlier in Reference 23 while assuming nonorthogonality of the ROM subscales; this is close to the algebraic subgrid scale approach described in Reference 24. In Reference 26, authors propose a reduced basis method by means of a velocity-only formulation, which has the advantage of avoiding instabilities in the reduced space by dealing only with the velocity unknown and recovering the pressure later as a postprocess.

The present contribution aims to expand on the line of work done in References 21 and 24 and apply it to the field of FSI where it is shown, by means of numerical examples, that by applying VMS stabilization in the reduced space, it is possible to obtain a fully reduced FSI problem capable of solving challenging benchmarks with exemplary accuracy. A secondary contribution is the methodology carried out to achieve FSI coupling and how we expand it toward a fully reduced interaction problem. We take advantage of our partitioned strongly coupled solution scheme to obtain snapshots of each domain independently and similarly obtain independent reduced basis for each domain. We remark on the fact that while it is possible to apply our methodology to more standard (fluid-solid) FOM-ROM or ROM-FOM configurations, the novelty is in using a fully ROM-ROM interaction problem.

The article is organized as follows: in Sections 2 and 3, we describe each particular formulation, the fluid and solid, respectively, in a short manner. In Section 4, we introduce the FSI formulation. Afterward, an overview of ROM will be given in Section 5, detailing our implementation. Numerical results are presented in Section 6 and finally conclusions close the article in Section 7.

## 2 | INCOMPRESSIBLE NAVIER-STOKES EQUATIONS

In the next section, we present the finite element approximation we employ to solve the incompressible Navier-Stokes equations. This approximation is what we call the full order model (FOM) for the fluid problem.

### 2.1 | Governing equations

Let $\Omega_{\mathrm{fl}}$ be the domain where the fluid flow takes place, with boundary $\Gamma_{\mathrm{fl}} = \Gamma_{\mathrm{D,fl}} \cup \Gamma_{\mathrm{N,fl}}$, where $\Gamma_{\mathrm{D,fl}}$ and $\Gamma_{\mathrm{N,fl}}$ are boundaries where Dirichlet and Neumann conditions are prescribed, respectively. Let $[0, t_{\mathrm{f}}]$ be the time interval of analysis. The incompressible Navier-Stokes equations can be written as finding a velocity-pressure pair $[\boldsymbol{u}, p] : \Omega_{\mathrm{fl}} \times [0, t_{\mathrm{f}}[ \to \mathbb{R}^d \times \mathbb{R}$, where $d$ is the space dimension, as the solution to the following equations:

$$
\begin{aligned}
\rho_{\mathrm{fl}} \partial_t \boldsymbol{u} - 2\mu_{\mathrm{fl}} \nabla \cdot \nabla^s \boldsymbol{u} + \rho_{\mathrm{fl}} \boldsymbol{u} \cdot \nabla \boldsymbol{u} + \nabla p = \rho_{\mathrm{fl}} \boldsymbol{f} \quad & \text{in } \Omega_{\mathrm{fl}}, \quad t \in ]0, t_{\mathrm{f}}[, \\
\nabla \cdot \boldsymbol{u} = 0 \quad & \text{in } \Omega_{\mathrm{fl}}, \quad t \in ]0, t_{\mathrm{f}}[, \\
\boldsymbol{u} = \boldsymbol{u}_{\mathrm{D}} \quad & \text{on } \Gamma_{\mathrm{D,fl}}, \quad t \in ]0, t_{\mathrm{f}}[, \\
\boldsymbol{n}_{\mathrm{fl}} \cdot \boldsymbol{\sigma}_{\mathrm{fl}} = \boldsymbol{t}_{\mathrm{fl}} \quad & \text{on } \Gamma_{\mathrm{N,fl}}, \quad t \in ]0, t_{\mathrm{f}}[,
\end{aligned}
$$

$$\boldsymbol{u} = \boldsymbol{u}^0 \quad \text{in } \Omega_{\text{fl}}, \quad t = 0,$$

where $\rho_{\text{fl}}$ is the fluid's density, $\mu_{\text{fl}}$ is the fluid's dynamic viscosity, $\nabla^s \boldsymbol{u}$ is the symmetrical part of the velocity gradient, $\boldsymbol{f}$ is the body acceleration vector, $\boldsymbol{\sigma}_{\text{fl}} = -p\boldsymbol{I} + 2\mu_{\text{fl}}\nabla^s \boldsymbol{u}$ is the fluid's Cauchy stress tensor ($\boldsymbol{I}$ being the identity tensor), $\boldsymbol{u}^0$ is a prescribed initial velocity, $\boldsymbol{u}_{\text{D}}$ is a prescribed velocity on the boundary $\Gamma_{\text{D,fl}}$, $\boldsymbol{t}_{\text{fl}}$ is a prescribed traction on the boundary $\Gamma_{\text{N,fl}}$, and $\boldsymbol{n}_{\text{fl}}$ is the normal to the boundary.

## 2.2 | Weak form

Let us introduce some standard notation. The space of functions whose absolute value has an integrable $p$ power ($p \geq 1$) in a domain $\Omega$ is denoted by $L^p(\Omega)$, and the space of functions whose distributional derivatives of order up to $m \geq 0$ belong to $L^2(\Omega)$ by $H^m(\Omega)$. The $L^2$ inner product in $\Omega$ (for scalars, vectors, or tensors) is denoted by $(\cdot, \cdot)$. The integral of the product of two functions defined in $\omega$ is $\langle \cdot, \cdot \rangle_\omega$, with the subscript omitted when $\omega = \Omega$; this definition includes the duality pairing. Given a Banach space $X$ of time dependent functions, $L^p(0, t_{\text{f}}; X)$ denotes the space of functions whose norm in $X$ is in $L^p(0, t_{\text{f}})$, $p \geq 1$.

Using this notation, we can introduce the spaces for the Navier-Stokes equations, where now $\Omega = \Omega_{\text{fl}}$. Let $\mathcal{V}_0 = \{\boldsymbol{v} \in H^1(\Omega_{\text{fl}})^d | \boldsymbol{v}|_{\Gamma_D} = \boldsymbol{0}\}$, $\mathcal{V}_D = \{\boldsymbol{v} \in H^1(\Omega_{\text{fl}})^d | \boldsymbol{v}|_{\Gamma_D} = \boldsymbol{u}_D\}$, $\mathcal{Q} = L^2(\Omega_{\text{fl}})$, $\mathcal{W}_0 = \mathcal{V}_0 \times \mathcal{Q}$, and $\mathcal{W}_D = \mathcal{V}_D \times \mathcal{Q}$. The weak form of the Navier-Stokes equations consists in finding $[\boldsymbol{u}, p] \in L^2(0, t_{\text{f}}; \mathcal{V}_D) \times L^1(0, t_{\text{f}}; \mathcal{Q})$ (or a distribution in time) such that:

$$(\rho_{\text{fl}}\partial_t \boldsymbol{u}, \boldsymbol{v}) - 2\mu_{\text{fl}}(\nabla^s \boldsymbol{u}, \nabla^s \boldsymbol{v}) + \rho_{\text{fl}}\langle \boldsymbol{u} \cdot \nabla \boldsymbol{u}, \boldsymbol{v} \rangle - (p, \nabla \cdot \boldsymbol{v}) = \langle \rho_{\text{fl}} \boldsymbol{f}, \boldsymbol{v} \rangle + \langle \boldsymbol{t}, \boldsymbol{v} \rangle_{\Gamma_{N,\text{fl}}}, \quad t \in ]0, t_{\text{f}}[, \tag{1}$$

$$(q, \nabla \cdot \boldsymbol{u}) = 0, \quad t \in ]0, t_{\text{f}}[, \tag{2}$$

$$(\boldsymbol{u}, \boldsymbol{v}) = (\boldsymbol{u}^0, \boldsymbol{v}), \quad t = 0, \tag{3}$$

for all $[\boldsymbol{v}, q] \in \mathcal{V}_0 \times \mathcal{Q}$. For $\boldsymbol{U} \equiv [\boldsymbol{u}, p] : ]0, t_{\text{f}}[ \rightarrow \mathcal{W}_D$ and $\boldsymbol{V} \equiv [\boldsymbol{v}, q] \in \mathcal{W}_0$, we can define the form $B$ as

$$B(\boldsymbol{U}, \boldsymbol{V}) = 2\mu_{\text{fl}}(\nabla^s \boldsymbol{u}, \nabla^s \boldsymbol{v}) + \rho_{\text{fl}}\langle \boldsymbol{u} \cdot \nabla \boldsymbol{u}, \boldsymbol{v} \rangle - (p, \nabla \cdot \boldsymbol{v}) + (q, \nabla \cdot \boldsymbol{u}),$$

and the linear form $L$ as

$$L(\boldsymbol{V}) = \langle \rho_{\text{fl}} \boldsymbol{f}, \boldsymbol{v} \rangle + \langle \boldsymbol{t}, \boldsymbol{v} \rangle_{\Gamma_{N,\text{fl}}},$$

which enable us to write (1) and (2) in the following simplified form:

$$(\rho_{\text{fl}}\partial_t \boldsymbol{u}, \boldsymbol{v}) + B(\boldsymbol{U}, \boldsymbol{V}) = L(\boldsymbol{V}) \quad \forall \boldsymbol{V} \in \mathcal{W}_0. \tag{4}$$

## 2.3 | Galerkin spatial discretization

For the spatial discretization, the standard Galerkin finite element approximation can be defined as follows. Let $\mathcal{P}_h$ denote a finite element partition of a domain $\Omega$. The diameter of an element domain $K \in \mathcal{P}_h$ is denoted by $h_K$ and the diameter of the finite element partition by $h = \max\{h_K | K \in \mathcal{P}_h\}$. In the case $\Omega = \Omega_{\text{fl}}$, we can now construct conforming finite element spaces $\mathcal{V}_h \subset \mathcal{V}_D$, $\mathcal{Q}_h \subset \mathcal{Q}$, and $\mathcal{W}_{h,D} = \mathcal{V}_h \times \mathcal{Q}_h$, as well as $\mathcal{V}_{h,0} \subset \mathcal{V}_0$ and $\mathcal{W}_{h,0} = \mathcal{V}_{h,0} \times \mathcal{Q}_h$, in the usual manner. Then the problem can be written as: find $\boldsymbol{U}_h : ]0, t_{\text{f}}[ \rightarrow \mathcal{W}_{h,D}$ as the solution to the problem:

$$\begin{aligned} (\rho_{\text{fl}}\partial_t \boldsymbol{u}_h, \boldsymbol{v}_h) + B(\boldsymbol{U}_h, \boldsymbol{V}_h) = L(\boldsymbol{V}_h) \quad \forall \boldsymbol{V}_h \in \mathcal{W}_{h,0}, \\ (\boldsymbol{u}_h, \boldsymbol{v}_h) = (\boldsymbol{u}^0, \boldsymbol{v}_h) \quad \forall \boldsymbol{v}_h \in \mathcal{V}_{h,0}, \quad t = 0. \end{aligned} \tag{5}$$

The convective term is linearized by means of a Picard linearization scheme.

## 2.4 | Time discretization

Let us consider a uniform partition of the time interval $]0, t_f[$ of size $\Delta t$, and let us denote with superscript $n$ the time level. For the temporal discretization, usual finite difference schemes can be adopted. In particular, we have used the second-order backward difference (BDF2) scheme, which has the following form:

$$\left.\frac{\partial \boldsymbol{u}_h}{\partial t}\right|_{t^{n+1}} = \frac{3\boldsymbol{u}_h^{n+1} - 4\boldsymbol{u}_h^{n} + \boldsymbol{u}_h^{n-1}}{\Delta t} + \mathcal{O}(\Delta t^2) =: \delta_{2,t}\boldsymbol{u}_h^{n+1} + \mathcal{O}(\Delta t^2),$$

where $t^k = k\Delta t$, $k = n-1, n, n+1$ .

## 2.5 | Stabilization

To circumvent the restrictions imposed by the inf-sup condition and convection dominated flows, a VMS stabilization is applied, originally proposed in[27] and later further developed in[28,29] (see also[30] for a review). When applied to the Navier-Stokes problem, the time discrete version of Equation (5) is replaced by:

$$\begin{aligned}(\rho_{\mathrm{fl}}\delta_{2,t}\boldsymbol{u}_h^{n+1}, \boldsymbol{v}_h) + B(\boldsymbol{U}_h^{n+1}, \boldsymbol{V}_h) + \sum_K \left\langle \tilde{\boldsymbol{u}}^{n+1}, \rho_{\mathrm{fl}}\boldsymbol{u}_h^{n+1}\cdot\nabla\boldsymbol{v}_h + \mu_{\mathrm{fl}}\Delta\boldsymbol{v}_h + \nabla q_h\right\rangle_K \\ - \sum_K \left\langle \tilde{p}^{n+1}, \nabla\cdot\boldsymbol{v}_h\right\rangle_K = L(\boldsymbol{V}_h),\end{aligned} \tag{6}$$

where $\tilde{\boldsymbol{u}}^{n+1}$ and $\tilde{p}^{n+1}$ are the solution of

$$\frac{\rho_{\mathrm{fl}}}{\Delta t}\left(\tilde{\boldsymbol{u}}^{n+1} - \tilde{\boldsymbol{u}}^{n}\right) + \frac{1}{\tau_1}\tilde{\boldsymbol{u}}^{n+1} = \Pi^{\perp}\left(\boldsymbol{r}\left(\boldsymbol{U}_h^{n+1}\right)\right), \tag{7}$$

$$\frac{1}{\tau_2}\tilde{p}^{n+1} = -\Pi^{\perp}\left(\nabla\cdot\boldsymbol{u}_h^{n+1}\right), \tag{8}$$

within each element domain $K$ of the finite element partition of the fluid domain, with

$$\begin{aligned}\boldsymbol{r}\left(\boldsymbol{U}_h^{n+1}\right) &= \rho_{\mathrm{fl}}\delta_{2,t}\boldsymbol{u}_h^{n+1} - \mu_{\mathrm{fl}}\Delta\boldsymbol{u}_h^{n+1} + \rho_{\mathrm{fl}}\boldsymbol{u}_h^{n+1}\cdot\nabla\boldsymbol{u}_h^{n+1} + \nabla p_h^{n+1} - \rho_{\mathrm{fl}}\boldsymbol{f}^{n+1},\\ \tau_1 &= \left[c_1\frac{\mu_{\mathrm{fl}}}{h^2} + c_2\frac{\rho_{\mathrm{fl}}|\boldsymbol{u}_h|_K}{h}\right]^{-1},\end{aligned} \tag{9}$$

$$\tau_2 = c_3\frac{h^2}{\tau_1}. \tag{10}$$

In Equations (7) and (8), $\Pi^{\perp}$ is the projection orthogonal to the finite element space (either of velocities or of pressures), computed as $\Pi^{\perp} = I - \Pi$, $\Pi$ being the projection onto the adequate finite element space. In Equations (9) and (10), $|\boldsymbol{u}_h|_K$ is the mean velocity modulus in element $K$, $h$ is the element size, and $c_1$, $c_2$, and $c_3$ are stabilization constants. For linear elements, we take $c_1 = 4.0$, $c_2 = 2.0$, and $c_3 = 1.0$; for quadratic elements, we use the same values but taking $h$ half the element size (roughly the distance between nodes of the element), as justified in Reference 31.

The method we use was introduced in Reference 29. It belongs to the VMS family, with the subgrid scales, that is, the components of the unknowns that cannot be reproduced by the finite element space, orthogonal to it, and time dependent; in fact, Equation (7) is an approximation to the exact subgrid scale equation using the backward Euler scheme to discretize in time.

# 3 | NONLINEAR SOLID ELASTODYNAMICS

In this section, a short review of the nonlinear solid elastodynamics formulation we employ is given, as well as the spatial and temporal discretization schemes used.

### 3.1 | Governing equations

Let $\Omega_{\text{sl}}$ be the domain of the solid, with boundary $\Gamma_{\text{sl}} = \Gamma_{\text{D,sl}} \cup \Gamma_{\text{N,sl}}$, where $\Gamma_{\text{D,sl}}$ and $\Gamma_{\text{N,sl}}$ are boundaries where Dirichlet and Neumann conditions are prescribed, respectively. The time interval of analysis $]0, t_{\text{f}}[$ is the same as for the fluid. The elastodynamics problem written in updated Lagrangian form[32] consists in finding a displacement field $\boldsymbol{d} : \Omega_{\text{sl}} \times ]0, t_{\text{f}}[ \rightarrow \mathbb{R}^d$ such that:

$$\begin{aligned}
\rho_{\text{sl}} \partial_{tt} \boldsymbol{d} - \nabla \cdot \boldsymbol{\sigma}_{\text{sl}} &= \rho_{\text{sl}} \boldsymbol{f} \quad \text{in } \Omega_{\text{sl}}, \quad t \in ]0, t_{\text{f}}[, \\
\boldsymbol{d} &= \boldsymbol{d}_{\text{D}} \quad \text{on } \Gamma_{\text{D,sl}}, \quad t \in ]0, t_{\text{f}}[, \\
\boldsymbol{n}_{\text{sl}} \cdot \boldsymbol{\sigma}_{\text{sl}} &= \boldsymbol{t}_{\text{sl}} \quad \text{on } \Gamma_{\text{N,sl}}, \quad t \in ]0, t_{\text{f}}[, \\
\partial_t \boldsymbol{d} &= \dot{\boldsymbol{d}}^0 \quad \text{in } \Omega_{\text{sl}}, \quad t = 0, \\
\boldsymbol{d} &= \boldsymbol{d}^0 \quad \text{in } \Omega_{\text{sl}}, \quad t = 0,
\end{aligned} \tag{11}$$

where $\rho_{\text{sl}}$ is the solid's density, $\boldsymbol{\sigma}_{\text{sl}}$ is the solid's Cauchy stress tensor, $\boldsymbol{f}$ is the acceleration vector of the solid (now defined on $\Omega_{\text{sl}}$), $\boldsymbol{d}^0$ is a prescribed initial displacement and $\dot{\boldsymbol{d}}^0$ is a prescribed initial velocity, $\boldsymbol{d}_D$ is a prescribed displacement on the boundary $\Gamma_{\text{D,sl}}$, $\boldsymbol{t}_{\text{sl}}$ is a prescribed traction on the boundary $\Gamma_{\text{N,sl}}$, and $\boldsymbol{n}_{\text{sl}}$ is the normal to the solid domain.

In the nonlinear setting, the constitutive equation for the stress tensor can be modeled in a variety of ways and depends on the material to be simulated. In the present case, we are interested in the Neo-Hookean and Saint Venant-Kirchoff material models, which can be defined as follows:

$$\begin{aligned}
\text{NeoHookean: } \boldsymbol{\sigma}_{\text{sl}} &= \frac{1}{J} \left[ \lambda_{\text{sl}} \ln(J) \boldsymbol{I} + \mu_{\text{sl}} (\boldsymbol{b} - \boldsymbol{I}) \right], \\
\text{Saint Venant-Kirchoff: } \boldsymbol{\sigma}_{\text{sl}} &= \frac{1}{J} \boldsymbol{F} \left[ \lambda_{\text{sl}} \text{tr}(\boldsymbol{E}) \boldsymbol{I} + 2\mu_{\text{sl}} \boldsymbol{E} \right] \boldsymbol{F}^T,
\end{aligned}$$

where $\boldsymbol{F} = \frac{\partial \boldsymbol{x}}{\partial \boldsymbol{X}}$ is the deformation gradient, $J = \det(\boldsymbol{F})$, $\lambda_{\text{sl}}$ and $\mu_{\text{sl}}$ are Lamé's parameters, $\boldsymbol{b} = \boldsymbol{F}\boldsymbol{F}^T$ is the left Cauchy tensor, $\boldsymbol{I}$ is the identity tensor, and $\boldsymbol{E}$ is the Green-Lagrange strain tensor.

### 3.2 | Weak form

Let $\mathcal{E}_0 = \{ \boldsymbol{e} \in H^1(\Omega_{\text{sl}})^d | \boldsymbol{e}|_{\Gamma_{\text{D}}} = \boldsymbol{0} \}$ and $\mathcal{E}_{\text{D}} \subset \{ \boldsymbol{e} \in H^1(\Omega_{\text{sl}})^d | \boldsymbol{e}|_{\Gamma_{\text{D}}} = \boldsymbol{d}_{\text{D}} \}$ be the appropriate spaces where the test functions and the displacement field (for $t \in ]0, t_{\text{f}}[$) should belong, respectively. The weak form of the solid elastodynamics problem consists in finding $\boldsymbol{d}$ in an adequate subspace of $L^2(0, t_{\text{f}}; \mathcal{E}_{\text{D}})$ such that:

$$\begin{aligned}
(\rho_{\text{sl}} \partial_{tt} \boldsymbol{d}, \boldsymbol{e}) - (\boldsymbol{\sigma}_{\text{sl}}, \nabla^s \boldsymbol{e}) &= \langle \rho_{\text{sl}} \boldsymbol{f}, \boldsymbol{e} \rangle + \langle \boldsymbol{t}_{\text{sl}}, \boldsymbol{e} \rangle_{\Gamma_{\text{N,sl}}}, \quad t \in ]0, t_{\text{f}}[, \\
(\partial_t \boldsymbol{d}, \boldsymbol{e}) &= (\dot{\boldsymbol{d}}^0, \boldsymbol{e}), \quad t = 0, \\
(\boldsymbol{d}, \boldsymbol{e}) &= (\boldsymbol{d}^0, \boldsymbol{e}), \quad t = 0,
\end{aligned} \tag{12}$$

for all $\boldsymbol{e} \in \mathcal{E}_0$.

### 3.3 | Spatial discretization

We can discretize the solid domain as done for the fluid and use also an analogous notation. In this way, we can now construct conforming finite element spaces $\mathcal{E}_{h,\text{D}} \subset \mathcal{E}_{\text{D}}$ and $\mathcal{E}_{h,0} \subset \mathcal{E}_0$. Then, the Galerkin finite element approximation can be written as finding $\boldsymbol{d}_h$ in the appropriate subspace of $L^2(0, t_{\text{f}}; \mathcal{E}_{h,\text{D}})$ such that:

$$\begin{aligned}
(\rho_{\text{sl}} \partial_{tt} \boldsymbol{d}_h, \boldsymbol{e}_h) - (\boldsymbol{\sigma}_{\text{sl},h}, \nabla^s \boldsymbol{e}_h) &= \langle \rho_{\text{sl}} \boldsymbol{f}, \boldsymbol{e}_h \rangle + \langle \boldsymbol{t}_{\text{sl}}, \boldsymbol{e}_h \rangle_{\Gamma_{\text{N,sl}}}, \quad t \in ]0, t_{\text{f}}[, \\
(\partial_t \boldsymbol{d}_h, \boldsymbol{e}_h) &= (\dot{\boldsymbol{d}}^0, \boldsymbol{e}_h), \quad t = 0, \\
(\boldsymbol{d}_h, \boldsymbol{e}_h) &= (\boldsymbol{d}^0, \boldsymbol{e}_h), \quad t = 0,
\end{aligned} \tag{13}$$

for all $\boldsymbol{e}_h \in \mathcal{E}_{h,0}$, where $\boldsymbol{\sigma}_{\text{sl},h}$ is the Cauchy stress tensor evaluated with $\boldsymbol{d}_h$. This problem can be linearized using a Newton-Raphson scheme; for further details see, for example, Reference 32.

### 3.4 | Time discretization

Even though any finite difference scheme in time could be used, including the popular Newmark scheme, in this work for the temporal discretization, the following BDF2 scheme has been used:

$$\boldsymbol{a}^{n+1} = \frac{1}{(\Delta t)^2}\left(2\boldsymbol{d}^{n+1} - 5\boldsymbol{d}^{n} + 4\boldsymbol{d}^{n-1} - \boldsymbol{d}^{n-2}\right),$$

where $\boldsymbol{d}^{n+1}$ and $\boldsymbol{a}^{n+1}$ are approximations to the position and acceleration vectors at time step $n+1$, respectively.

## 4 | FLUID STRUCTURE INTERACTION

Once all ingredients have been identified, it is possible to detail the process of dealing with FSI problems. In this section, we first express the FSI equations in weak form, and then we detail the FSI algorithm as well as the boundary relaxation scheme used.

### 4.1 | Governing equations and weak form

The approach followed in this work can be taken as the traditional one in a broad sense, where an updated Lagrangian formulation is used to deal with the solid mechanics problem, while the fluid problem is solved by means of an Arbitrary-Lagrangian-Eulerian (ALE) formulation[33] to cope with the domain motion.

Borrowing the notation developed in previous sections, we can expand it to account for a moving domain and to take into account the interaction between subdomains. We will use a superscript $t$ to indicate the time dependency of the spaces and a temporal argument for the geometrical domains. For the FSI problem, the space for the continuous problem can be defined as $\mathcal{F}_{D,t} = \mathcal{W}_{D,t} \times \mathcal{E}_{D,t}$, and the initial and boundary value problem can be stated as finding $[\boldsymbol{u}, p, \boldsymbol{d}] \in L^2(0, t_\mathrm{f}; \mathcal{V}_{D,t}) \times L^1(0, t_\mathrm{f}; \mathcal{Q}_{D,t}) \times L^2(0, t_\mathrm{f}; \mathcal{E}_{D,t})$ such that:

$$\begin{aligned}
&\rho_\mathrm{fl}(\partial_t \boldsymbol{u}, \boldsymbol{v}) - 2\mu_\mathrm{fl}(\nabla^s \boldsymbol{u}, \nabla^s \boldsymbol{v}) \\
&\quad + \rho_\mathrm{fl}\langle \boldsymbol{c}\cdot\nabla\boldsymbol{u}, \boldsymbol{v}\rangle - (p, \nabla\cdot\boldsymbol{v}) = \langle \rho_\mathrm{fl}\boldsymbol{f}, \boldsymbol{v}\rangle + \langle \boldsymbol{t}_\mathrm{fl}, \boldsymbol{v}\rangle_{\Gamma_{\mathrm{N,fl}}} \quad \text{in } \Omega(t)_\mathrm{fl}, \quad t \in ]0, t_\mathrm{f}[, \\
&\qquad (q, \nabla\cdot\boldsymbol{u}) = 0 \quad \text{in } \Omega(t)_\mathrm{fl}, \quad t \in ]0, t_\mathrm{f}[, \\
&\qquad (\rho_\mathrm{sl}\partial_{tt}\boldsymbol{d}, \boldsymbol{e}) - (\boldsymbol{\sigma}_\mathrm{sl}, \nabla^s \boldsymbol{e}) = \langle \rho_\mathrm{sl}\boldsymbol{f}, \boldsymbol{e}\rangle + \langle \boldsymbol{t}_\mathrm{sl}, \boldsymbol{e}\rangle_{\Gamma_{\mathrm{N,sl}}} \quad \text{in } \Omega(t)_\mathrm{sl}, \quad t \in ]0, t_\mathrm{f}[, \\
&\qquad\qquad \boldsymbol{u} = \partial_t \boldsymbol{d} \quad \text{on } \Gamma(t)_\mathrm{I}, \quad t \in ]0, t_\mathrm{f}[, \\
&\qquad\qquad \boldsymbol{n}_\mathrm{sl}\cdot\boldsymbol{\sigma}_\mathrm{sl} + \boldsymbol{n}_\mathrm{fl}\cdot\boldsymbol{\sigma}_\mathrm{fl} = \boldsymbol{0} \quad \text{on } \Gamma(t)_\mathrm{I}, \quad t \in ]0, t_\mathrm{f}[,
\end{aligned} \tag{14}$$

for all $[\boldsymbol{v}, q, \boldsymbol{e}] \in \mathcal{F}_{0,t}$, with $\mathcal{F}_{0,t} = \mathcal{W}_{0,t} \times \mathcal{E}_{0,t}$, and satisfying initial conditions in a weak sense. In the momentum equation for the fluid, $\boldsymbol{c}$ is known as the convection velocity from the domain point of view, which is given by $\boldsymbol{c} = \boldsymbol{u} - \boldsymbol{u}_\mathrm{domain}$, where $\boldsymbol{u}_\mathrm{domain}$ is the velocity of the points in the computational domain to which the unknowns are referred. Note that in this form, the domains to which the fluid and solid pertain, $\Omega(t)_\mathrm{fl}$ and $\Omega(t)_\mathrm{sl}$, respectively, are now time dependent, as they change according to the deformation process. The boundary $\Gamma(t)_\mathrm{I}$ is the interface for both domains.

The finite element approximation and integration in time of problem (14) follows the lines described in Sections 2 and 3 for each subproblem, and we shall not detail this further. It only remains to indicate how to treat numerically the transmission conditions, and this depends on the coupling scheme described next.

From now on, we will consider that the unknowns have been discretized, although we shall not introduce the subscript $h$ to lighten the notation. In particular, we shall refer to $\boldsymbol{u}_\mathrm{domain}$ as the mesh velocity, $\boldsymbol{u}_\mathrm{mesh}$, as the points in the domain will be moved according to the velocity computed for the mesh nodes. The mesh movement algorithm that we have employed has been taken from Reference 34, which has proven simple, robust, and reliable. The only restriction that $\boldsymbol{u}_\mathrm{mesh}$ has to satisfy is that it must be equal to the velocity of the boundary of the fluid domain at this boundary.

### 4.2 | Coupling scheme

There are various ways to treat the numerical system for the interaction problem regardless of the particular formulation used to solve each domain. In a monolithic coupling, the whole problem is assembled and solved, coupling is

treated implicitly.[35,36] This approach benefits from increased stability on the solution but requires a solver specially tailored for coupled FSI problems. On the other hand, partitioned approaches assemble each domain independently and coupling is achieved through right-hand-side terms of each system that need to be guessed. For strongly coupled systems, subiterations, and very often relaxation, are necessary to guarantee convergence on the interaction boundaries. In some cases, a high number of coupling iterations are necessary to achieve convergence.[37,38] Finally, a less popular approach is to use a staggered coupling (or loosely coupled interaction); this is essentially a partitioned approach where the boundary conditions are treated explicitly and no subiterations are done. This approach can suffer from instabilities, like the added mass effect; see[39] for a comprehensive discussion on the added mass effect on partitioned coupled solvers.[40]

In this work, we employ a partitioned strongly coupled scheme to achieve domain coupling; this means that for every time-step each domain is iterated independently until convergence is achieved for velocity, pressure, and displacement on the interaction boundary. This creates the necessity of an additional iteration loop that guarantees coupling convergence. In total, we are left with three coupling blocks, these being the internal solver convergence, the nonlinearity convergence of each problem (fluid and solid), and the coupling convergence for the interaction boundary. This is clarified in Section 4.3. In our implementation, iteration by subdomain can be done for nonmatching meshes by means of the Lagrange interpolation functions to ensure continuity of certain quantities, as shown in Reference 41.

The order in which we iterate is the standard one, the one that guarantees stability of the process due to the different "stiffnesses" of the subproblems, namely, a Dirichlet-Neumann coupling. The way to proceed is to determine the shape of the fluid domain from the deformation obtained at a certain iteration within a given time step for the solid, as well as the velocity of the domain boundary; from this, one can compute the velocity of the mesh in the fluid domain and solve the flow equations. Once velocities and pressures in the fluid are computed, the resulting normal stress on the solid boundary can be obtained, and this can be used to solve the problem in the solid domain. The process needs to be repeated until convergence is achieved. This guarantees that both transmission conditions in problem (14) will hold.

In the process described, relaxation of the transmitted quantities is very often required if not mandatory. This allows one to minimize the number of block (fluid and solid) iterations. In this respect, we have used a relaxation of the position and velocity of the interface boundary that the solid solver transmits to the fluid solver. We denote this position as $\boldsymbol{d}_{\Gamma_I}$; from it, one may compute the velocity of the fluid boundary and $\boldsymbol{u}_{\text{mesh}}$, as explained above. We have implemented an Aitken relaxation scheme, in particular Aitken $\Delta^2$, detailed in Reference 42, which we describe now in our context. Within each time step, let us denote by a superscript $k$ the $k$th block-iteration of any variable. For clarity, let us omit the superscript with the time step counter. Suppose that from values at the $k$th iteration, the solid is solved, obtaining the boundary displacements $\boldsymbol{d}^{k+1}_{\Gamma_I,\text{sl}}$. Then, the fluid is solved from the boundary displacements $\boldsymbol{d}^{k+1}_{\Gamma_I}$ computed as

$$\boldsymbol{d}^{k+1}_{\Gamma_I} = \boldsymbol{d}^{k}_{\Gamma_I} + \omega^{k+1}\boldsymbol{r}^{k+1}_{\Gamma_I}, \tag{15}$$

where

$$\boldsymbol{r}^{k+1}_{\Gamma_I} := \boldsymbol{d}^{k+1}_{\Gamma_I,\text{sl}} - \boldsymbol{d}^{k}_{\Gamma_I}, \tag{16}$$

$$\omega^{k+1} = -\omega^{k}\frac{(\boldsymbol{r}^{k}_{\Gamma_I})^T(\boldsymbol{r}^{k+1}_{\Gamma_I} - \boldsymbol{r}^{k}_{\Gamma_I})}{|\boldsymbol{r}^{k+1}_{\Gamma_I} - \boldsymbol{r}^{k}_{\Gamma_I}|^2}. \tag{17}$$

## 4.3 | General FSI algorithm

For a time interval between 0 and $t_f$, let $n$ be the current time step, $n_{\text{last}}$ is the last time step, $i$ is the current internal iteration of a particular subdomain (fluid or solid), $k$ is the current coupling iteration for both domains, $\text{Tol}_{\text{time}}$ is the temporal tolerance (to decide whether the steady state has been reached or not), $\text{Tol}_{\text{cou}}$ is the coupling tolerance between subdomains, $\text{Tol}_{\text{sl}}$ is the internal tolerance for convergence for the solid subdomain, and $\text{Tol}_{\text{fl}}$ is the internal tolerance for convergence for the fluid subdomain. The FSI algorithm is displayed in Algorithm 1. For $i = 0$ (either for the fluid or for the solid), the unknowns are initialized to those of the previous block-iteration, whereas for $k = 0$, they are initialized to those of the previous time step.

**Algorithm 1.** General FSI algorithm

Read case parameters and initialize values for the fluid and the solid domains
**for** $n = 1; n \leq n_{\text{last}}; n + 1$ **do**
  **for** $k = 1; k \leq k_{\max}; k + 1$ **do**
    **for** $i = 1; i \leq i_{\max}; i + 1$ **do**
      Solve the fluid problem for $[\boldsymbol{u}_h, p_h]^{i+1}$ from $\boldsymbol{u}^k_{\text{mesh}}$
      Calculate error $\epsilon^{i+1}_{\boldsymbol{u}} = \frac{|\boldsymbol{u}^{i+1}_h - \boldsymbol{u}^i_h|}{|\boldsymbol{u}^{i+1}_h|}; \epsilon^{i+1}_p = \frac{|p^{i+1}_h - p^i_h|}{|p^{i+1}_h|}; \epsilon^{i+1}_{\boldsymbol{u}}$ and $\epsilon^{i+1}_{\boldsymbol{p}} \leq \text{Tol}_{\text{fl}}$
      Nonlinearity converged; break nonlinearity loop
    **end for**
    Set $[\boldsymbol{u}_h, p_h]^{k+1} \leftarrow [\boldsymbol{u}_h, p_h]^{i+1}$
    Calculate tractions $\boldsymbol{t}^{k+1}_{\text{fl}}$ on $\Gamma_{\text{I}}$ (to be transmitted to the solid)
    **for** $i = 1; i \leq i_{\max}; i + 1$ **do**
      Solve the solid problem for $\boldsymbol{d}^{i+1}_h$ from $\boldsymbol{t}^{k+1}_{\text{fl}}$
      Calculate error $\epsilon^{i+1}_{\boldsymbol{d}} = \frac{|\boldsymbol{d}^{i+1}_h - \boldsymbol{d}^i_h|}{|\boldsymbol{d}^{i+1}_h|} \epsilon^{i+1}_{\boldsymbol{d}} \geq \text{Tol}_{\text{sl}}$
      Nonlinearity converged; break nonlinearity loop
    **end for**
    Set $\boldsymbol{d}^{k+1}_h \leftarrow \boldsymbol{d}^{i+1}_h$ and $\boldsymbol{d}^{k+1}_{\Gamma_{\text{I}},\text{sl}}$ the values of $\boldsymbol{d}^{k+1}_h$ on $\Gamma_{\text{I}}$
    Calculate the residual on the $\boldsymbol{r}^{k+1}_{\Gamma_{\text{I}}}$ from (16)
    Calculate the relaxation parameter $\omega^{k+1}$ from (17)
    Calculate the mesh interface movement $\boldsymbol{d}^{k+1}_{\Gamma_{\text{I}}} = \boldsymbol{d}^k_{\Gamma_{\text{I}}} + \omega^{k+1} \boldsymbol{r}^{k+1}_{\Gamma_{\text{I}}}$
    Calculate the fluid mesh movement $\boldsymbol{d}^{k+1}_{\text{mesh}}$ and the fluid mesh velocity $\boldsymbol{u}^{k+1}_{\text{mesh}}$ from $\boldsymbol{d}^{k+1}_{\Gamma_{\text{I}}}$
    Calculate the coupling error $\epsilon^{k+1}_{\boldsymbol{u}} = \frac{|\boldsymbol{u}^{k+1}_h - \boldsymbol{u}^k_h|}{|\boldsymbol{u}^{k+1}_h|}; \epsilon^{k+1}_p = \frac{|p^{k+1}_h - p^k_h|}{|p^{k+1}_h|}; \epsilon^{k+1}_{\boldsymbol{d}} = \frac{|\boldsymbol{d}^{k+1}_h - \boldsymbol{d}^k_h|}{|\boldsymbol{d}^{k+1}_h|} \epsilon^{k+1}_{\boldsymbol{u}}$ and $\epsilon^{k+1}_p$ and $\epsilon^{k+1}_{\boldsymbol{d}}$ on $\Gamma_{\text{I}} \leq \text{Tol}_{\text{coup}}$
    Coupling converged; break coupling loop
  **end for**
  Calculate temporal increment $\epsilon^{n+1}_{\boldsymbol{u}} = \frac{|\boldsymbol{u}^{n+1}_h - \boldsymbol{u}^n_h|}{|\boldsymbol{u}^{n+1}_h|}; \epsilon^{n+1}_p = \frac{|p^{n+1}_h - p^n_h|}{|p^{n+1}_h|}; \epsilon^{n+1}_{\boldsymbol{d}} = \frac{|\boldsymbol{d}^{n+1}_h - \boldsymbol{d}^n_h|}{|\boldsymbol{d}^{n+1}_h|} \epsilon^{n+1}_{\boldsymbol{u}}$ and $\epsilon^{n+1}_p$ and $\epsilon^{n+1}_{\boldsymbol{d}} \leq \text{Tol}_{\text{time}}$
  Stationary state achieved; break temporal loop
**end for**
Finalize case
Output if necessary

## 5 | REDUCED ORDER MODELING

As discussed in Section 4.2, strongly coupled partitioned FSI algorithms may require a high number of subiterations and subrelaxation, making the problem potentially expensive numerically and consequently taking a long time to achieve a solution. In this sense, the development of model order reduction schemes that increase performance while maintaining output accuracy is of interest. Herein lies our motivation to introduce ROM into FSI. In this section, we give a short review of the methodology we apply and the algorithmic aspects that concern it.

It is, however, convenient to give a wider framework for our proposed ROM strategy. As mentioned earlier, the stabilization of the reduced space problem is not a new field of research. In Reference 43, the concept of an inf-sup compatible ROM formulation is introduced, enhancing stability by the addition of what the authors call *supremizer* terms to the reduced formulation. The supremizer permits the enforcement of the incompressibility in the process by adding new DOF for the velocity. It is seen that solving exactly for the exact supremizer during the online stage becomes unfeasible so the recommended approach is to actually develop this calculation offline, apply POD, obtain a basis for the supremizer unknowns, and treat it as any other reduced variable. The authors achieve a stable ROM by the addition of a few supremizer terms into the system. Later, this idea was extended in Reference 25 to the field of FSI by adding a VMS stabilization into the reduced space for the fluid, similar to what had previously been done in Reference 23, the main difference being the type of stabilization.

## 5.1 | Some ROM theory and notation

Let us define a high-dimensional space $\mathcal{Y}_h$ of dimension $M$, with $\boldsymbol{\varphi} = \{\boldsymbol{\varphi}^1, \dots, \boldsymbol{\varphi}^M\}$ its orthonormal basis, whose elements are vectors of $D$ components. Then any element $\boldsymbol{y}_h \in \mathcal{Y}_h$ can be written as the linear combination $\boldsymbol{y}_h = \sum_{k=1}^{M} (\boldsymbol{y}_h, \boldsymbol{\varphi}^k)\boldsymbol{\varphi}^k$, now with $(\cdot,\cdot)$ is the $L^2$-inner product in $\mathcal{Y}_h$. We can also define a low-dimensional subspace $\mathcal{Y}_{\text{rom}} \subset \mathcal{Y}_h$ of dimension $m$, which approximates $\mathcal{Y}_h$ as $m \to M$, with a basis $\boldsymbol{\phi} = \{\boldsymbol{\phi}^1, \dots, \boldsymbol{\phi}^m\}$. Using this basis, we can approximate any element $\boldsymbol{y}_h$ as $\boldsymbol{y}_h \approx \boldsymbol{y}_{\text{rom}} = \sum_{k=1}^{m} \boldsymbol{\phi}^k a^k$, where $a^k$ is the $k$th coefficient which can be computed as $a^k = (\boldsymbol{y}_h, \boldsymbol{\phi}^k)$, and which will typically be obtained from the solution of the reduced problem. The accuracy of the approximation depends on how well the basis $\boldsymbol{\phi}$ approximates the exact basis $\boldsymbol{\varphi}$. As we use a nested basis scheme, a finer basis includes the previous one within its space.

### 5.1.1 | Construction of the basis

The method we use to construct the basis of the low-dimensional space is the POD. The objective of this method is finding a basis from a collection of high-fidelity "snapshots," which in our context are solutions in $\mathcal{Y}_h$ of an evolution problem at certain time steps. As it is well known, we need to subtract the mean. Thus, taking a set of data as a collection of $N$ snapshots $\{\boldsymbol{s}_j\}_{j=1}^N = \{\boldsymbol{y}_{h,j} - \bar{\boldsymbol{y}}_h\}_{j=1}^N$, the overbar denoting the mean of the $\boldsymbol{y}_{h,j} \in \mathcal{Y}_h$, we can reproduce any element of this collection as

$$\boldsymbol{y}_{h,j} \approx \bar{\boldsymbol{y}}_h + \sum_{k=1}^{m} (\boldsymbol{s}_j, \boldsymbol{\phi}^k)\boldsymbol{\phi}^k, \tag{18}$$

where, in the case of POD, $\{\boldsymbol{\phi}^k\}_{k=1}^m$ is an orthonormal system of $\mathcal{Y}_h$. The POD consists in finding the orthonormal basis $\{\boldsymbol{\phi}^k\}_{k=1}^m$ of $\mathcal{Y}_{\text{rom}}$ such that:

$$\begin{aligned} \min_{\{\boldsymbol{\phi}\}_{k=1}^m} \quad & \frac{1}{N}\sum_{j=1}^{N} \left\| \boldsymbol{s}_j - \sum_{k=1}^{m} (\boldsymbol{s}_j, \boldsymbol{\phi}^k)\boldsymbol{\phi}^k \right\|^2, \\ \text{subject to} \quad & (\boldsymbol{\phi}^i, \boldsymbol{\phi}^j) = \delta_{ij}, \quad 1 \le i,j \le m, \end{aligned} \tag{19}$$

where $\|\cdot\|$ denotes the $L^2$ norm. By means of a singular value decomposition (SVD), we can solve for the basis $\{\boldsymbol{\phi}^k\}_{k=1}^m$ from the matrix of snapshots. This basis depends on parameters as time-step, how often the snapshots were acquired and the reproducibility of the function being analyzed. A reduced basis can be defined by truncating the left singular-vectors at the $m$th column. As a criterion for the truncation, we use the retained energy $\eta$, defined in Reference 15 as:

$$\eta = \frac{\sum_{k=1}^{m} \lambda^k}{\sum_{k=1}^{M} \lambda^k}, \tag{20}$$

where $\{\lambda^k\}_{k=1}^M$ are the singular values of the SVD. The SVD produces a diagonal matrix which contains, from greatest to smallest, the eigenvalues of the associated (singular) eigen-vectors. The ordering of the eigenvalues is a measure of the relative importance of each of the basis functions in the whole system. In general, in a reducible problem (a problem that should be easily reproduced by means of ROM), they decrease quickly in magnitude. If $m$ is sufficiently small, the time to compute the reduced system is minimal.

The stage of the problem in which the basis is calculated is termed as the off-line phase.

*Remark* 1. The snapshots are arrays of $M$ components, and therefore the vectors of the ROM basis are also arrays of $M$ components. In our finite element context, however, we may identify them as piecewise polynomial functions. Indeed, if $\phi^{k,a}$ is the $a$th component of the $k$th basis vector, $a = 1, \dots, M$, we may identify $\boldsymbol{\phi}^k$ with the function

$$\phi^k(\boldsymbol{x}) = \sum_{a=1}^{M} N^a(\boldsymbol{x})\phi^{k,a}, \quad k = 1, \dots, m,$$

where $\boldsymbol{x}$ is the position vector and $N^a(\boldsymbol{x})$ the finite element interpolation function of the $a$th degree of freedom. Therefore, $\mathcal{Y}_{\text{rom}}$ can be identified as a space of functions of dimension $m$.

In the case of FSI problems, the construction of the basis can be done in a variety of ways, as shown in Reference 12 for domain decomposition problems. In our case, and as a first approach, it was decided to assemble and calculate the snapshots of each subdomain separately, that is, the basis for the fluid domain from the snapshots of velocity and pressure in the fluid ($\boldsymbol{\phi}_{\text{fl}}(\boldsymbol{u}_h, p_h)$) and the basis for the solid domain from the snapshots of displacements ($\boldsymbol{\phi}_{\text{sl}}(\boldsymbol{d}_h)$). However, it is also possible to construct and assemble just one basis from the joint snapshots of velocity, pressure, and displacement ($\boldsymbol{\phi}_{\text{fl,sl}}(\boldsymbol{u}_h, p_h, \boldsymbol{d}_h)$); the performance of this option is left for future study (see Reference 12 for further details).

### 5.1.2 | Variational multiscale-reduced order model

In FSI problems and with the partitioned strategy we have followed, we have to solve one variational problem in the fluid domain and another one in the solid domain. The Galerkin finite element approximation to these problems can be stated as these variational problems restricted to the finite element spaces, both for the unknowns and for the test functions. In a similar way, the ROM could be expressed as the same variational problems, now restricting unknowns and test functions to the ROM spaces, with a much smaller dimension than the finite element spaces. There are other options to state the ROM problem, but the approach described justifies that one may expect similar instability problems for the Galerkin finite element method and the described Galerkin-ROM. Therefore, some sort of numerical stabilization will be required *for the fluid problem*. The solid problem we have considered (without incompressibility of mixed formulations) does not require any stabilization; the Galerkin method yields a stable and accurate approximation.

The approach we shall follow for the fluid is the same as for the finite element problem, namely, to use a VMS method with an approximation to the subgrid scales similar to that given by (7). In the ROM case, it is particularly natural to use *orthogonal* subgrid scales, since the vectors of the basis are mutually orthogonal. Therefore, if the ROM space is obtained by truncating the vectors obtained from a SVD of the collection of snapshots to the first $m$ members, the space of subgrid scales is simply its $L^2$-orthogonal complement.

Let $\boldsymbol{U}_{\text{rom}} \equiv [\boldsymbol{u}_{\text{rom}}, p_{\text{rom}}] : ]0, t_{\text{f}}[ \to \mathcal{Y}_{\text{rom}}$ and $\boldsymbol{V}_{\text{rom}} \equiv [\boldsymbol{v}_{\text{rom}}, q_{\text{rom}}] \in \mathcal{Y}_{\text{rom}}$ be the ROM unknown and test functions of the fluid problem, respectively, where $\mathcal{Y}_{\text{rom}}$ is the velocity-pressure pair obtained from the POD basis (using its interpretation as a function space described in Remark 1). According to the previous considerations, and using the BDF2 scheme for the time discretization, the problem we have to solve for the ROM is:

$$\begin{aligned}(\rho_{\text{fl}}\delta_{2,t}\boldsymbol{u}_{\text{rom}}^{n+1}, \boldsymbol{v}_{\text{rom}}) + B(\boldsymbol{U}_{\text{rom}}^{n+1}, \boldsymbol{V}_{\text{rom}}) + \sum_K \left\langle \check{\boldsymbol{u}}^{n+1}, \rho_{\text{fl}}\boldsymbol{u}_{\text{rom}}^{n+1}\cdot\nabla\boldsymbol{v}_{\text{rom}} + \mu_{\text{fl}}\Delta\boldsymbol{v}_{\text{rom}} + \nabla q_{\text{rom}}\right\rangle_K \\ - \sum_K \left\langle \check{p}^{n+1}, \nabla\cdot\boldsymbol{v}_{\text{rom}}\right\rangle_K = L(\boldsymbol{V}_{\text{rom}}),\end{aligned} \tag{21}$$

where $\check{\boldsymbol{u}}^{n+1}$ and $\check{p}^{n+1}$ are the solution of

$$\frac{\rho_{\text{fl}}}{\Delta t}\left(\check{\boldsymbol{u}}^{n+1} - \check{\boldsymbol{u}}^{n}\right) + \frac{1}{\tau_1}\check{\boldsymbol{u}}^{n+1} = \Pi_{\text{rom}}^{\perp}\left(\boldsymbol{r}\left(\boldsymbol{U}_{\text{rom}}^{n+1}\right)\right), \tag{22}$$

$$\frac{1}{\tau_2}\check{p}^{n+1} = -\Pi_{\text{rom}}^{\perp}\left(\nabla\cdot\boldsymbol{u}_{\text{rom}}^{n+1}\right), \tag{23}$$

within each element domain $K$ of the finite element partition of the fluid domain, with

$$\boldsymbol{r}\left(\boldsymbol{U}_{\text{rom}}^{n+1}\right) = \rho_{\text{fl}}\delta_{2,t}\boldsymbol{u}_{\text{rom}}^{n+1} - \mu_{\text{fl}}\Delta\boldsymbol{u}_{\text{rom}}^{n+1} + \rho_{\text{fl}}\boldsymbol{u}_{\text{rom}}^{n+1}\cdot\nabla\boldsymbol{u}_{\text{rom}}^{n+1} + \nabla p_{\text{rom}}^{n+1} - \rho_{\text{fl}}\boldsymbol{f}^{n+1},$$

and the stabilization parameters computed as in Equations (9) and (10), replacing $\boldsymbol{u}_h$ by $\boldsymbol{u}_{\text{rom}}$ in the former. In Equations (22) and (23), $\Pi_{\text{rom}}^{\perp} = I - \Pi_{\text{rom}}$, where $\Pi_{\text{rom}}$ is the $L^2$-projection onto the appropriate ROM space (of velocities or of pressures).

*Remark* 2. Note that we make use of the finite element partition, both in problem (21) and in the definition of the stabilization parameters. This is possible because the ROM basis vectors can be understood as piecewise polynomial functions defined on each element of the partition (see Remark 1).

*Remark* 3. Contrary to Reference 21, the space where the subscales belong is directly $L^2$-orthogonal to the ROM space, whereas in the cited reference it is a subspace of the finite element space.

As a concluding remark to this section, we would like to address our choice of not using modal analysis based methods, which is usually the norm in ROM for solids. It is clear that fluid flow is impossible to be represented via this kind of eigenvalue decomposition, specially for the highly nonlinear nature of the flows we are interested in. Even though it is possible to represent the nonlinearities present in structural dynamics by modal analysis, as it is mentioned in Reference 20, a basis calculated by this approach needs to be recalculated very often to guarantee that the solution will reproduce accurately nonlinear behavior. Our approach focuses on the idea of "one-for-all" methodology, where by means of one robust formulation any kind of problem can be represented. In conclusion, we apply the same form of decomposition (namely, POD) to both the fluid and the structure.

## 5.2 | The algorithm

We describe next the algorithm to solve FSI problems using ROM for both the fluid and the solid, which we denote as ROM-ROM algorithm. However, we first describe the modifications that need to be done in the FOM, that we denote FOM-FOM algorithm, to obtain the necessary data for the ROM-ROM case.

### 5.2.1 | FOM-FOM case

Algorithm 2, essentially the same as in Algorithm 1 but with minor differences, corresponds to the off-line phase of a simulation case. We make use of all variables and parameters previously defined and add $\boldsymbol{\phi}_{\text{fl}}$ and $\boldsymbol{\phi}_{\text{sl}}$; these are the fluid and solid basis, respectively. The dots represent the parts that are the same as in Algorithm 1.

**Algorithm 2.** FOM-FOM algorithm previous to a ROM-ROM calculation

Read case parameters and initialize values for fluid and solid domains, number of snapshots to take and parameters for the SVD solver
**for** $n = 1; n \leq n_{\text{last}}; n + 1$ **do**
  **for** $k = 1; k \leq k_{\max}; k + 1$ **do**
    ...
    **for** $i = 1; i \leq i_{\max}; i + 1$ **do**
      Solve fluid domain ...
    **end for**
    **for** $i = 1; i \leq i_{\max}; i + 1$ **do**
      Solve solid domain ...
    **end for**
    ...$\epsilon_{\boldsymbol{u}}^{k+1}$ and $\epsilon_{p}^{k+1}$ and $\epsilon_{\boldsymbol{d}}^{k+1}$ on $\Gamma_{\text{I}} \leq \text{Tol}_{\text{coup}}$
    Store snapshot of $\boldsymbol{u}^{n+1}, p^{n+1}$ if required
    Store snapshot of $\boldsymbol{d}^{n+1}$ if required
    Coupling converged; Break Coupling loop
  **end for**
  ...
**end for**
Finalize case
Calculate bases $\boldsymbol{\phi}_{\text{fl}}$, $\boldsymbol{\phi}_{\text{sl}}$ by solving problem (19)
Output if necessary

*Remark* 4. This process is most efficiently done taking full advantage of parallel solving, both for the FOM and ROM versions of the case. This means that the basis can be calculated and written to disk in parallel as well.

### 5.2.2 | ROM-ROM case

Algorithm 3 shows the ROM phase for the coupled problem, also known as the on-line phase. We make use of all the parameters defined in Section 5.2.1 and add $[\overline{\boldsymbol{u}}, \overline{p}, \overline{\boldsymbol{d}}]$, which are the snapshot mean values for the fluid and solid unknowns

(velocity-pressure and displacements). In essence, it is the same as Algorithm 1 replacing finite element unknowns by ROM unknowns.

**Algorithm 3.** ROM-ROM algorithm

Read case parameters and initialize values for fluid and solid domains
**Initialize Fluid problem**: read previously calculated reduced basis $\boldsymbol{\phi}_{\text{fl}}$, and select the desired amount of basis vectors through any criterion (energy for example).
**Initialize Solid problem**: read previously calculated reduced basis $\boldsymbol{\phi}_{\text{sl}}$, and select the desired amount of basis vectors through any criterion (energy for example).
**for** $n = 1; n \leq n_{\text{last}}; n+1$ **do**
  **for** $k = 1; k \leq k_{\max}; k+1$ **do**
    **for** $i = 1; i \leq i_{\max}; i+1$ **do**
      Write $[\boldsymbol{u}_{\text{rom}}, p_{\text{rom}}]^{i+1}$ in terms of $\boldsymbol{\phi}_{\text{fl}}$ and $[\bar{\boldsymbol{u}}, \bar{p}]$
      Solve the fluid problem for $[\boldsymbol{u}_{\text{rom}}, p_{\text{rom}}]^{i+1}$ from $\boldsymbol{u}^{k}_{\text{mesh}}$
      Calculate error $\epsilon^{i+1}_{\boldsymbol{u}} = \frac{|\boldsymbol{u}^{i+1}_{\text{rom}} - \boldsymbol{u}^{i}_{\text{rom}}|}{|\boldsymbol{u}^{i+1}_{\text{rom}}|}$; $\epsilon^{i+1}_{p} = \frac{|p^{i+1}_{\text{rom}} - p^{i}_{\text{rom}}|}{|p^{i+1}_{\text{rom}}|}$;$\epsilon^{i+1}_{\boldsymbol{u}}$ and $\epsilon^{i+1}_{\boldsymbol{p}} \leq \text{Tol}_{\text{fl}}$
      Nonlinearity converged; break nonlinearity loop
    **end for**
    Set $[\boldsymbol{u}_{\text{rom}}, p_{\text{rom}}]^{k+1} \leftarrow [\boldsymbol{u}_{\text{rom}}, p_{\text{rom}}]^{i+1}$
    Calculate tractions $\boldsymbol{t}^{k+1}_{\text{fl}}$ on $\Gamma_{\text{I}}$ (to be transmitted to the solid)
    **for** $i = 1; i \leq i_{\max}; i+1$ **do**
      Write $\boldsymbol{d}^{i+1}_{\text{rom}}$ in terms of $\boldsymbol{\phi}_{\text{sl}}$ and $\bar{\boldsymbol{d}}$
      Solve the solid problem for $\boldsymbol{d}^{i+1}_{\text{rom}}$ from $\boldsymbol{t}^{k+1}_{\text{fl}}$
      Calculate error $\epsilon^{i+1}_{\boldsymbol{d}} = \frac{|\boldsymbol{d}^{i+1}_{\text{rom}} - \boldsymbol{d}^{i}_{\text{rom}}|}{|\boldsymbol{d}^{i+1}_{\text{rom}}|}\epsilon^{i+1}_{\boldsymbol{d}} \geq \text{Tol}_{\text{sl}}$
      Nonlinearity converged; break nonlinearity loop
    **end for**
    Set $\boldsymbol{d}^{k+1}_{\text{rom}} \leftarrow \boldsymbol{d}^{i+1}_{\text{rom}}$ and $\boldsymbol{d}^{k+1}_{\Gamma_{\text{I}},\text{sl}}$ the values of $\boldsymbol{d}^{k+1}_{\text{rom}}$ on $\Gamma_{\text{I}}$
    Calculate the residual on the $\boldsymbol{r}^{k+1}_{\Gamma_{\text{I}}}$ from (16)
    Calculate relaxation parameter $\omega^{k+1}$ from (17)
    Calculate mesh interface movement $\boldsymbol{d}^{k+1}_{\Gamma_{\text{I}}} = \boldsymbol{d}^{k}_{\Gamma_{\text{I}}} + \omega^{k+1}\boldsymbol{r}^{k+1}_{\Gamma_{\text{I}}}$
    Calculate the fluid mesh movement $\boldsymbol{d}^{k+1}_{\text{mesh}}$ and fluid mesh velocity $\boldsymbol{u}^{k+1}_{\text{mesh}}$ from $\boldsymbol{d}^{k+1}_{\Gamma_{\text{I}}}$
    Calculate coupling error $\epsilon^{k+1}_{\boldsymbol{u}} = \frac{|\boldsymbol{u}^{k+1}_{\text{rom}} - \boldsymbol{u}^{k}_{\text{rom}}|}{|\boldsymbol{u}^{k+1}_{\text{rom}}|}$; $\epsilon^{k+1}_{p} = \frac{|p^{k+1}_{\text{rom}} - p^{k}_{\text{rom}}|}{|p^{k+1}_{\text{rom}}|}$; $\epsilon^{k+1}_{\boldsymbol{d}} = \frac{|\boldsymbol{d}^{k+1}_{\text{rom}} - \boldsymbol{d}^{k}_{\text{rom}}|}{|\boldsymbol{d}^{k+1}_{\text{rom}}|}\epsilon^{k+1}_{\boldsymbol{u}}$ and $\epsilon^{k+1}_{p}$ and $\epsilon^{k+1}_{\boldsymbol{d}}$ on $\Gamma_{\text{I}} \leq \text{Tol}_{\text{coup}}$
    Coupling converged; break coupling loop
  **end for**
  Calculate temporal increment $\epsilon^{n+1}_{\boldsymbol{u}} = \frac{|\boldsymbol{u}^{n+1}_{\text{rom}} - \boldsymbol{u}^{n}_{\text{rom}}|}{|\boldsymbol{u}^{n+1}_{\text{rom}}|}$; $\epsilon^{n+1}_{p} = \frac{|p^{n+1}_{\text{rom}} - p^{n}_{\text{rom}}|}{|p^{n+1}_{\text{rom}}|}$; $\epsilon^{n+1}_{\boldsymbol{d}} = \frac{|\boldsymbol{d}^{n+1}_{\text{rom}} - \boldsymbol{d}^{n}_{\text{rom}}|}{|\boldsymbol{d}^{n+1}_{\text{rom}}|}\epsilon^{n+1}_{\boldsymbol{u}}$ and $\epsilon^{n+1}_{p}$ and $\epsilon^{n+1}_{\boldsymbol{d}} \leq \text{Tol}_{\text{time}}$
  Stationary state achieved; break temporal loop
**end for**
Finalize case
Output if necessary

Due to the nonlinearity of both the solid and the fluid problem, it is necessary to assemble the linear system of unknowns at each iteration in the reduced order problem. This is a costly procedure, as it involves the whole array of unknowns (of the full order problem) and in general it is not scalable. Therefore, it is critical to think about *hyperreduction* as a means to placate this issue. This is usually done by selecting some critical points which represent accurately enough the nonlinear terms. There are various available techniques to do this, like Gappy-POD,[44] APHR,[45] or the GNAT method, the coarse-mesh-based hyperreduction proposed in Reference 46, to name a few.[47] We have not used any of these techniques in the examples to be shown in the next section: the utilization of an hyperreduction strategy will be addressed in future works; in this work, we have opted to focus our effort in the development of a stable and accurate formulation for FSI problems, without the added difficulty of finding a suitable and stable hyperreduction technique.

## 6 | NUMERICAL RESULTS

In this section, results of the FSI-ROM-ROM formulation proposed are shown. Two problems have been analyzed which exemplify two cases of interest, this being a semistationary case and a fully transient FSI case. For the fluid domain generally plots of integral quantities are preferred (lift and/or drag), pressure in the case of the semistationary case. For the solid domain displacement and acceleration plots are usually shown. A Fourier transform of the results is presented whenever deemed necessary.

Regarding the ROM problem, results are presented comparing the ROM result with the FOM result for the same case, using the basis that produced the most accurate results. Basis energy percentage is used for comparison between ROM results. Notice that in this work, each case consists of two reduced problems, for the solid and for the fluid, each with its particular basis taken from a different amount of snapshots.

It was observed that the ROM cases require a greater stabilization of the incompressibility term than the FOM cases to guarantee accurate results. For all FOM cases, the algorithmic constant in Equation (10) has been taken as $c_3 = 1.0$. In Section 6.2, we explore the effect of a slight variation of this constant.

### 6.1 | Semistationary bending of FSI plate

This 2D semistationary problem, taken from Reference 48, consists of a clamped plate perpendicular to the fluid flow. Once the flow starts from the left wall, it will bend the plate. For the particular conditions of the test, a steady state for the plate is achieved, in which it is bent without oscillating. In the fluid, only the vortices created at the tip of the plate are transient.

The test conditions are shown in Table 1 (SI units are assumed everywhere). In this example, all ROM cases have been solved using the constant $c_3 = 2.0$ in the ROM equation corresponding to Eq. (10).

Figure 1 shows the geometry and mesh for the test, where $H = 20$, $L = 80$, $h = 1$, $l = 10$.

Table 2 shows important mesh parameters and Table 3 shows the boundary conditions.

Out of experimentation it was found that ROM results that accurately represent the FOM are obtained when 99.999999% of the energy of the fluid is kept, amounting to 150 basis vectors, and 99.999999% of the energy of the solid base is taken, amounting to 36 basis vectors. ROM results are presented for this case. From the results, it can be seen that if fewer modes are retained the ROM solution starts to deviate from the FOM; this can be seen as well in the spectrum decay of the results. When fewer modes are used the low-energy high-frequency modes are not approximated correctly and noise is generated in that part of the spectrum (Figure 8B).

**TABLE 1** Physical parameters

| | Fluid | | Solid |
|---|---|---|---|
| $\rho_{\text{fl}}$ | 2.0 | $\rho_{\text{sl}}$ | 10.0 |
| $\mu_{\text{fl}}$ | 0.2 | $\mu_{\text{sl}}$ | 5000 |
| | | $\lambda_{\text{sl}}$ | 2000 |
| Model | Newtonian | | Neo-Hookean |

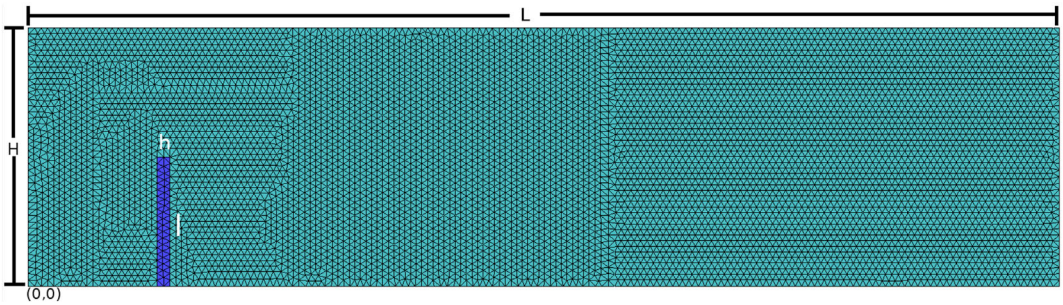


**FIGURE 1** Geometry and mesh used for semi-stationary FSI-ROM case [Colour figure can be viewed at wileyonlinelibrary.com]

**TABLE 2** Mesh parameters

| | Fluid | Solid |
|---|---|---|
| Element type | Quadratic triangle | Quadratic triangle |
| Nodes per element | 6 | 6 |
| # of elements | 14 308 | 78 |
| # of nodes | 29 057 | 201 |

**TABLE 3** Boundary conditions

| Fluid | Solid |
|---|---|
| $x = 0$: $u_x = 1, u_y = 0$ | $y = 0$: $d_x = d_y = 0$ |
| $y = 0, H$: free slip | Other boundaries: fluid tractions |
| $x = L$: free | |
| Other boundaries: solid velocities | |

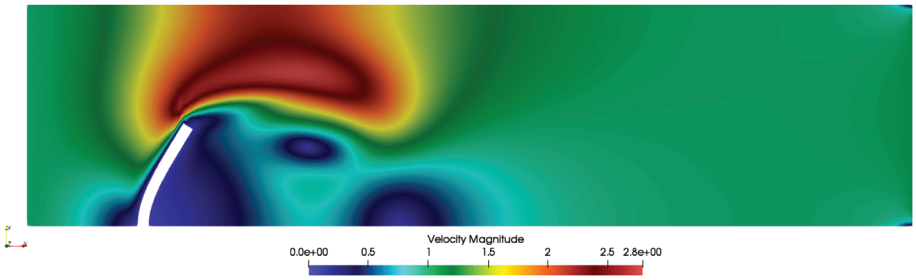


**FIGURE 2** Full order model: velocity

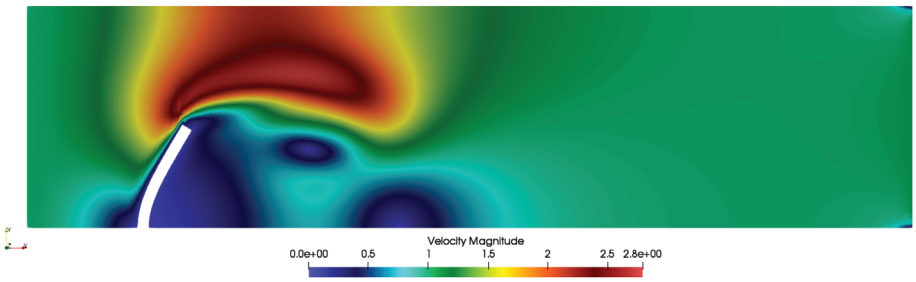


**FIGURE 3** ROM : Velocity

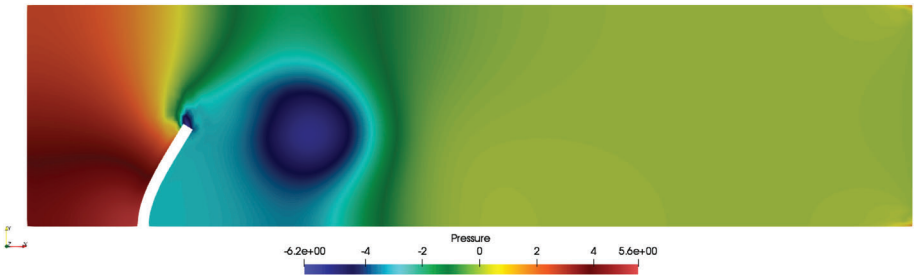


**FIGURE 4** Full order model: pressure

Note that from Table 2, it can be calculated that for the fluid problem the amount of DOF is 87 171, while for the solid it is 402. For the reduced problem we have 150 DOF for the fluid and 36 for the solid. This means that overall in terms of DOF we are achieving a reduction of 99.83% for the fluid and 91.05% for the solid, for a total reduction of 99.79%.

Figures 2 and 3 show contour plots for velocity and Figures 4 and 5 show contour plots for pressure for the final time of analysis, $t_f = 10.0$ seconds. Figure 6 shows displacement contours in the solid.

Both solutions, FOM and ROM, are very similar for both the fluid and the solid. Differences can be better observed in the next plots, in which we also consider the dependency on the time interval of analysis with which

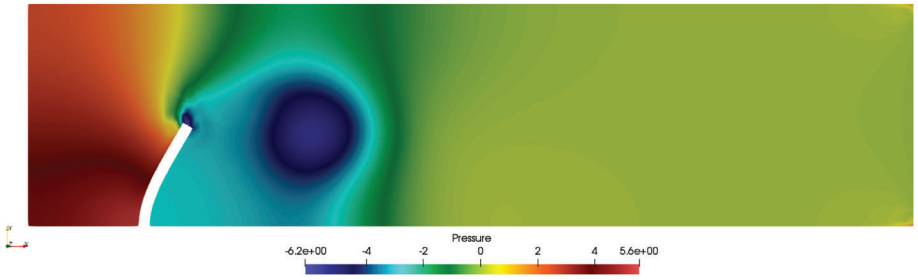


**FIGURE 5** Reduced order model: Pressure

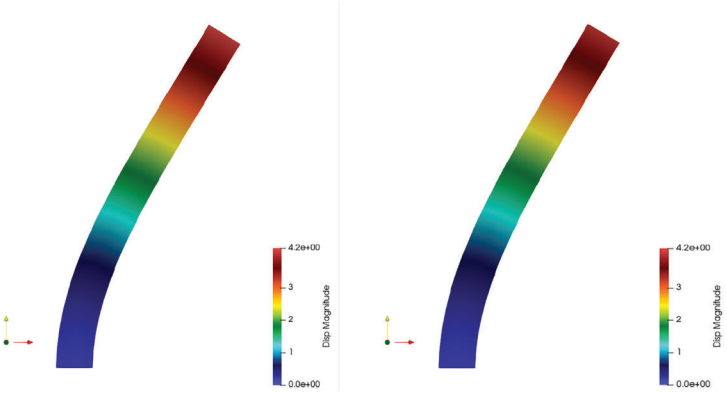


**FIGURE 6** Displacement magnitude for the solid bar. Left: full order model and right: ROM

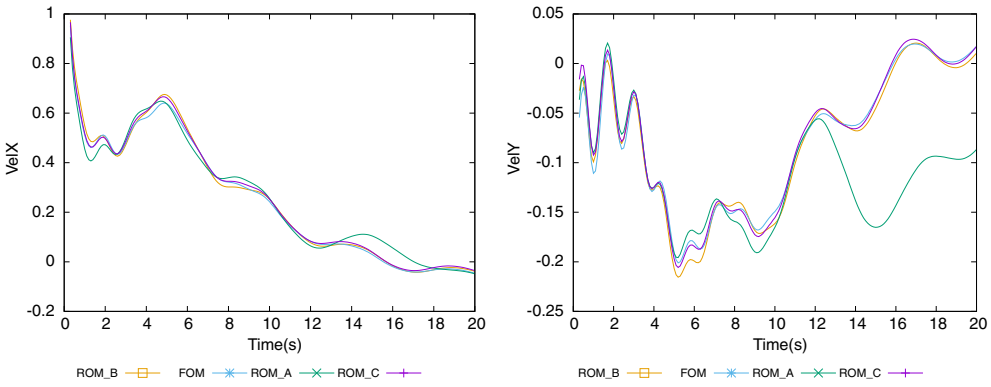


(A) Velocity in $x$ axis (B) Velocity in $y$ axis

**FIGURE 7** $x$ and $y$ velocities above the plate [Colour figure can be viewed at wileyonlinelibrary.com]

snapshots to construct the ROM basis are taken. Results are shown for three particular cases, labeled ROM_A, ROM_B, and ROM_C, leading to three different ROM basis. These are $\boldsymbol{\phi}_{\text{ROM\_A}}$, with a time interval $(0, 10)$, $\boldsymbol{\phi}_{\text{ROM\_B}}$, with a time interval $(0, 20)$, and $\boldsymbol{\phi}_{\text{ROM\_C}}$, with a time interval $(0, 40)$. In all cases, snapshots were taken each time step.

Figures 7 and 8 show the velocity components and pressure at a point in the fluid above the solid. Notice the importance of sampling the long stationary that develops after time $t = 12$. Even though cases ROM_B and ROM_C produce similar results, Figure 8B (the fast Fourier transform [FFT], of the pressure history) highlights that ROM_C yields a more stable and smoother solution.

Figure 9 shows the displacement of the tip of the plate; once again it is important to notice that lack of sampling of the stationary part of the solution makes the ROM inaccurate only in this region.

Figures 10 and 11 show the acceleration and its FFT at the tip of the plate. The analysis of the acceleration of the solid has been found to be critical, specially for FSI cases. Through experimentation we have found that when an adequate approximation of the acceleration is obtained (continuous and stable), we may expect an accurate and stable approximation of the whole solid domain. Results shown in the next section further support our claims, specially in the discussion around Figures 21 and 25.

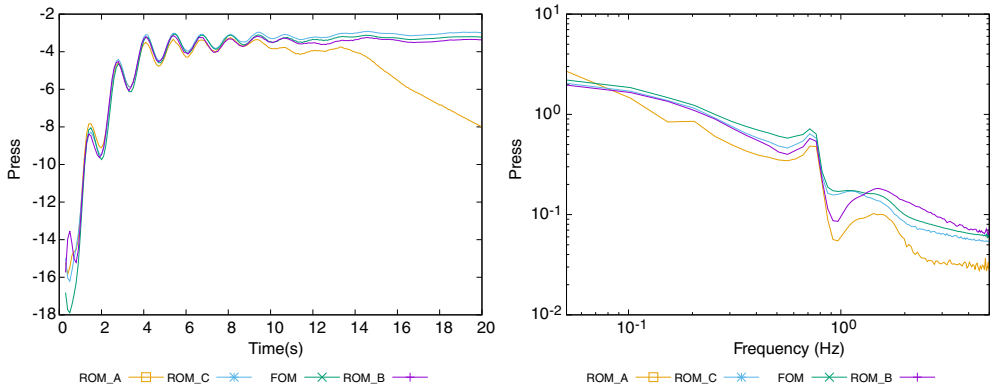


(A) Pressure (B) Pressure FFT

**FIGURE 8** Pressure and its fast Fourier transform around the plate [Colour figure can be viewed at wileyonlinelibrary.com]

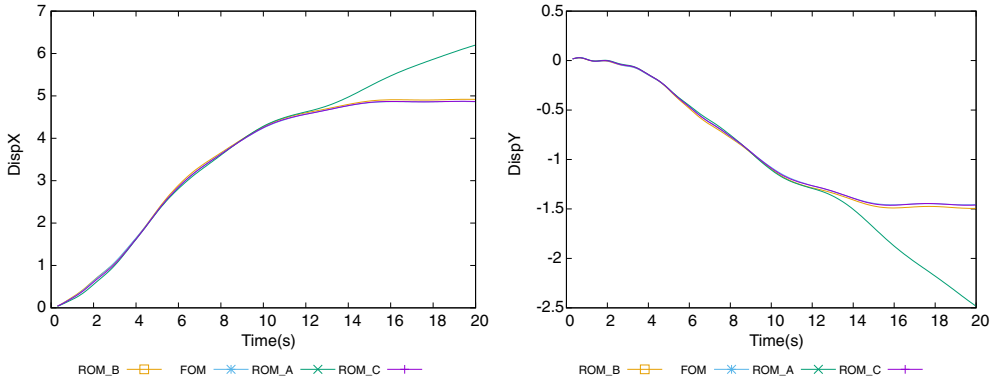


(A) Displacement in $x$ axis (B) Displacement in $y$ axis

**FIGURE 9** Displacement of the tip of the plate [Colour figure can be viewed at wileyonlinelibrary.com]

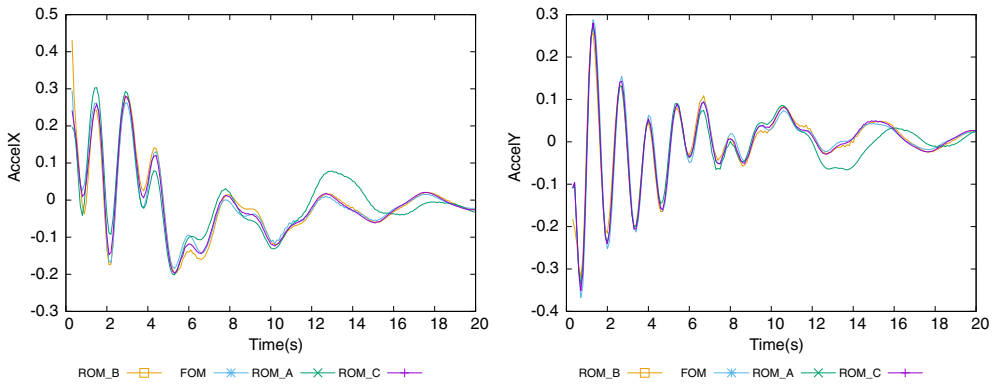


(A) Acceleration in $x$ axis (B) Acceleration in $y$ axis

**FIGURE 10** Acceleration of the tip of the plate [Colour figure can be viewed at wileyonlinelibrary.com]

## 6.2 | Flow around a cylinder with supported flag

The following example reproduces the benchmark presented in Reference 49, where a fluid flows around a cylinder with a supported flag. The fluid flows from the left wall and the tractions of the fluid onto the solid initiate the flag motion. After a while this motion is significant enough to move the fluid around it, starting a feedback loop between fluid and solid. The test conditions are shown in Table 4.

Figures 12 and 13 show the geometry and the finite element mesh used in this example. Note that the solid and fluid meshes are nonconforming, making the use of interpolation between subdomains necessary as discussed in Section 4.2. The length of the fluid domain is $L = 2.5$, its height $H = 0.41$, and the radius of the cylinder is $R = 0.05$. The length of the bar is $l = 0.35$ and its thickness $h = 0.02$.

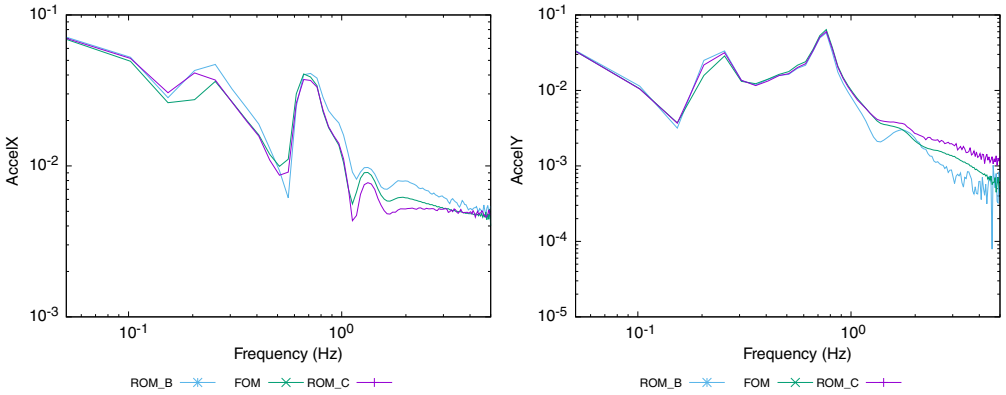


**FIGURE 11** Fast Fourier transform of the acceleration of the tip of the plate [Colour figure can be viewed at wileyonlinelibrary.com]

(A) Acceleration FFT in $x$ axis

(B) Acceleration FFT in $y$ axis

**TABLE 4** Physical parameters

| | Fluid | | Solid |
|---|---|---|---|
| $\rho_{\text{fl}}$ | 1000.0 | $\rho_{\text{sl}}$ | 10 000.0 |
| $\mu_{\text{fl}}$ | 0.001 | $\mu_{\text{sl}}$ | $0.5 \times 10^6$ |
| | | $\lambda_{\text{sl}}$ | $2.0 \times 10^6$ |
| Model | Newtonian | | St.Venant-Kirchoff |


**FIGURE 12** Geometry [Colour figure can be viewed at wileyonlinelibrary.com]

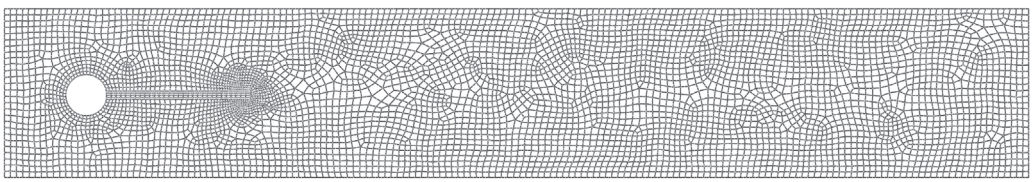

**FIGURE 13** Nonconforming mesh

Figure 14 shows a zoom for the cylinder and bar.

Tables 5 and 6 show important mesh parameters and boundary conditions, respectively.

Out of experimentation it was found that ROM results that accurately represent the FOM are obtained when 99.999999% of the energy of the fluid is taken, amounting to 163 basis vectors, and 99.999999% of the energy of the solid is taken, amounting to 48 basis vectors. From the results, it can be seen that if fewer modes are retained the ROM solution starts to deviate from the FOM; this can be seen as well in the spectrum decay of the results. In the same way as previously described, when fewer modes are used the low-energy high-frequency modes are not approximated correctly and noise is generated in that part of the spectrum (see Figure 25 and the discussion at the end of this section). Results for a basis using 99.9999% of the energy are also shown in the following, in this case using 158 basis vectors for the fluid and 16 for the solid.

Notice that from Table 5 it can be calculated that for the fluid problem the amount of DOF is 67 926, while for the solid it is 4422. For the reduced problem, we have 163 DOF for the fluid and 48 for the solid. This means that overall in terms of DOF we are achieving a reduction of 99.76% for the fluid and 98.91% for the solid, for a total reduction of 99.71%.

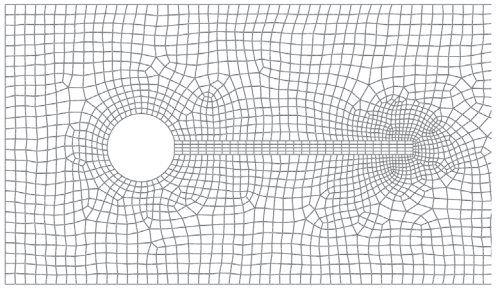

**FIGURE 14** Nonconforming mesh—zoom

**TABLE 5** Mesh parameters

| | Fluid | Solid |
|---|---|---|
| Element type | Quadratic quads | Quadratic quads |
| Nodes per element | 9 | 9 |
| # elements | 5531 | 500 |
| # nodes | 22 642 | 2211 |

**TABLE 6** Boundary conditions

| | Fluid | Solid |
|---|---|---|
| $x = 0$: | $u_x = 35.693\,y(0.41 - y)$, $u_y = 0.0$ | |
| $y = 0, H$: | Free slip | |
| $x = L$: | Free (zero traction) | |
| Cylinder boundary: | No slip | |
| Flag boundary: | Solid velocity | Fluid tractions |
| Flag-cylinder union: | | $d_x = d_y = 0$ |

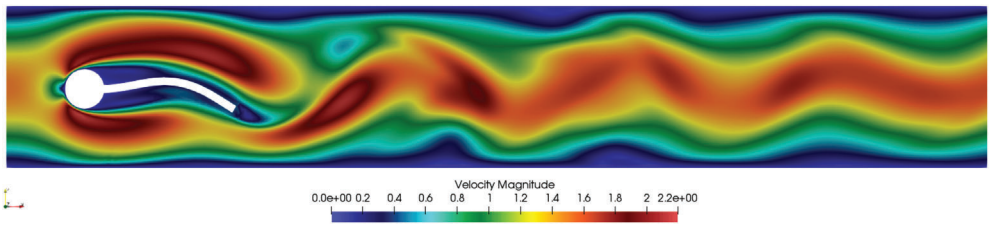


**FIGURE 15** Full order model: velocity magnitude

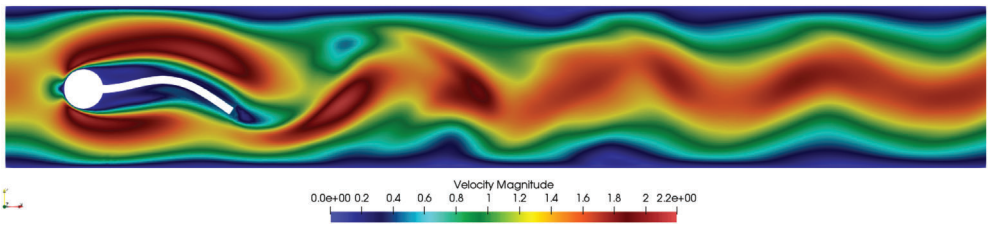


**FIGURE 16** Reduced order model: velocity magnitude

Figures 15 to 18 show contours for velocity and pressure, for both the reduced order problem and the full order problem at the last time of the simulation, $t = 1.2$. After this, graphs of significant quantities are compared for both the reduced and full order problems.

Figures 15 and 16 show velocity contours, Figures 17 and 18 show pressure contours, and Figure 19 shows the strain contours for the solid domain for both problems. In all cases, solutions are very similar.

Out of the many results that can be shown, it is considered valuable to see the dependency of the ROM result on the energy percentage used. Results are shown for three particular cases, labeled ROM_A, ROM_B, and ROM_C, which

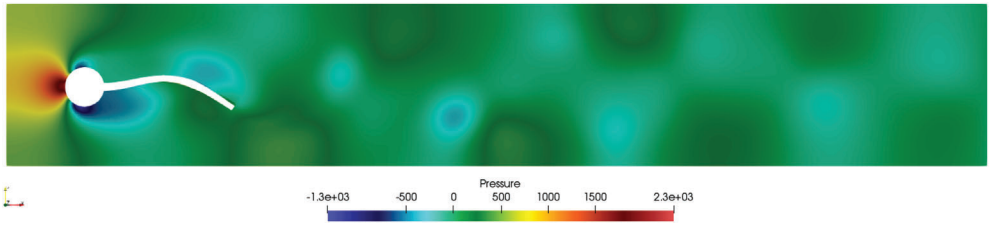


**FIGURE 17** Full order model: pressure

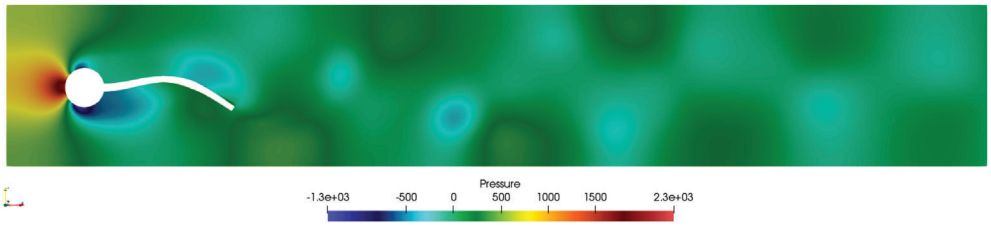


**FIGURE 18** Reduced order model: pressure

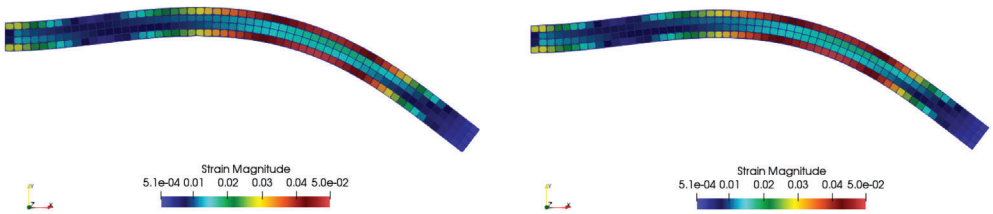


**FIGURE 19** Strain magnitude for the solid bar. Left: full order model and right: ROM

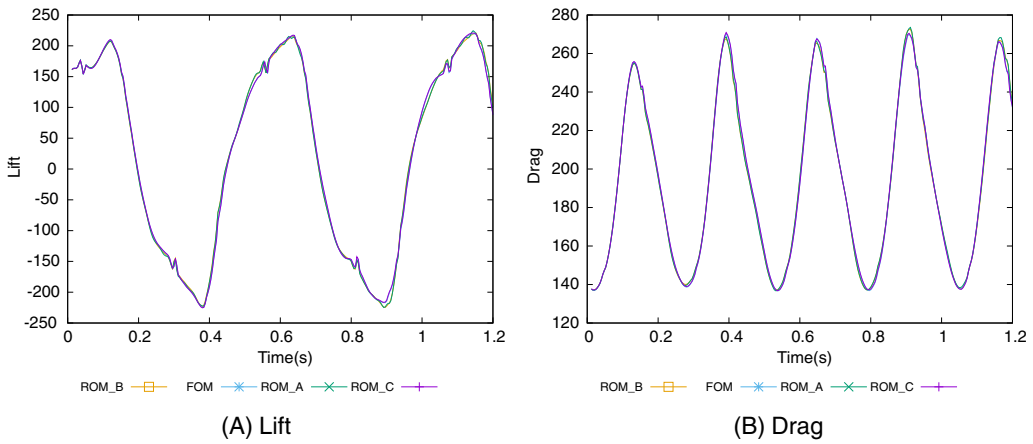


**FIGURE 20** Lift and drag around the flag [Colour figure can be viewed at wileyonlinelibrary.com]

correspond to $\eta = 99.9999\%$ the first two and $\eta = 99.999999\%$ the last one. The bases for all three cases were obtained sampling every time-step the FOM solution to collect the snapshots. While cases ROM_A and ROM_B share the same basis and same energy percentage, the difference between them is the stabilization constant for the incompressibility term of the Navier-Stokes equation (see Equation (10)). In this example, we explore the effect of a slight variation in constant $c_3$. For case ROM_A, we have used $c_3 = 1.5$, while for case ROM_B, we have taken $c_3 = 2.0$.

Figure 20 shows the drag and lift around the geometry of the flag caused by the fluid. Unlike the example shown in Section 6.1, this test case is much more complex and requires much more computational time as well as a richer basis to produce meaningful results. Given that the results are very similar, it is instructive to see a zoom for the lift, shown in Figure 21, where it is evident that a slight variation of the stabilization coefficient for the incompressibility directly affects the accuracy of the results.

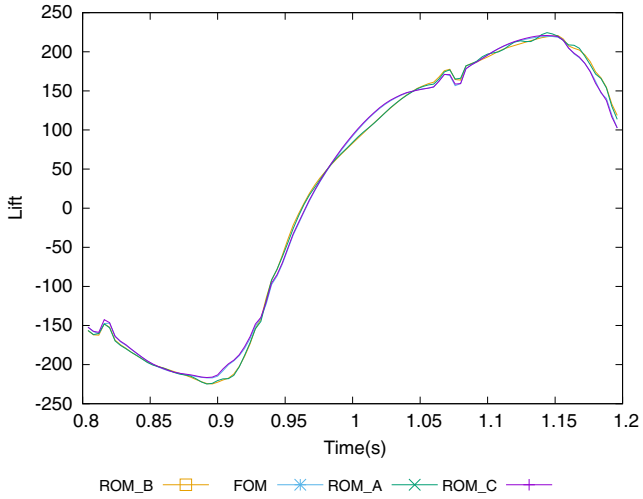


**FIGURE 21** Zoom for lift [Colour figure can be viewed at wileyonlinelibrary.com]

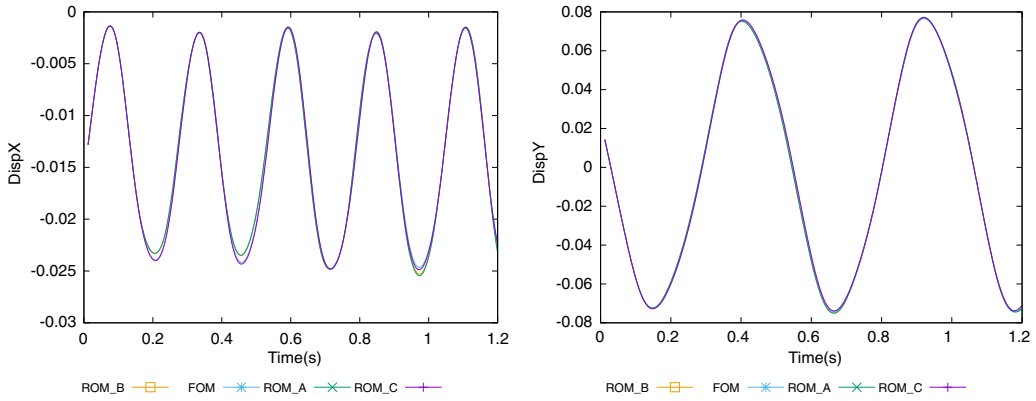


(A) Displacement in $x$ axis (B) Displacement in $y$ axis

**FIGURE 22** Displacement at the tip of the flag [Colour figure can be viewed at wileyonlinelibrary.com]

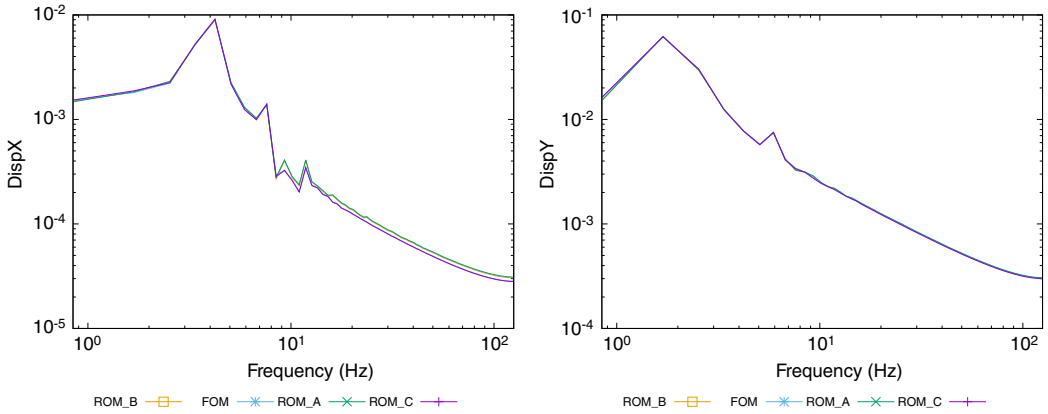


(A) Displacement FFT in $x$ axis (B) Displacement FFT in $y$ axis

**FIGURE 23** Fast Fourier transform of the displacement at the tip of the flag [Colour figure can be viewed at wileyonlinelibrary.com]

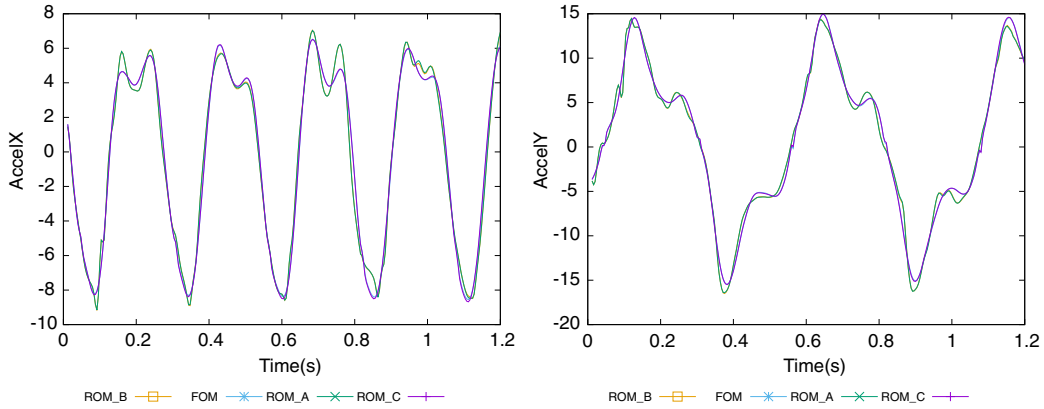


(A) Acceleration in $x$ axis (B) Acceleration in $y$ axis

**FIGURE 24** Acceleration at the tip of the flag [Colour figure can be viewed at wileyonlinelibrary.com]

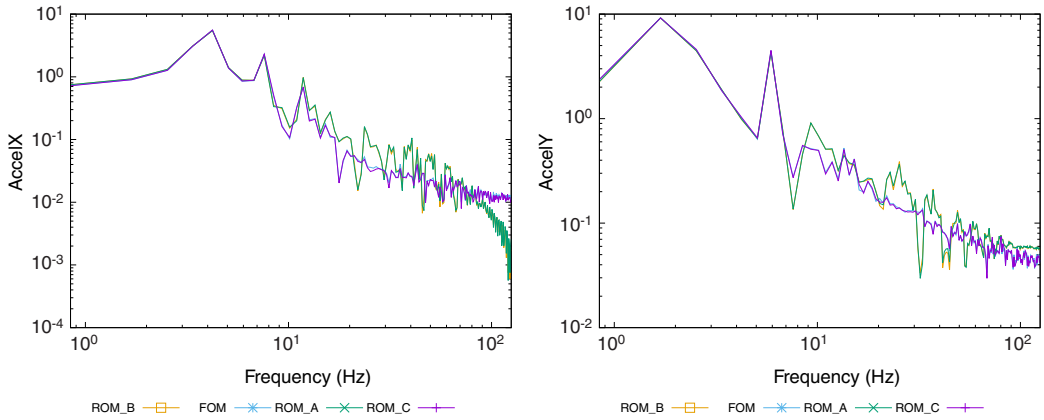


(A) Acceleration FFT in $x$ axis (B) Acceleration FFT in $y$ axis

**FIGURE 25** Fast Fourier transform of the acceleration at the tip of the flag [Colour figure can be viewed at wileyonlinelibrary.com]

**TABLE 7** Time and speedup for fluid and solid domains

| | | FOM | ROM_A | ROM_B | ROM_C |
|---|---|---|---|---|---|
| Fluid | Time (min) | 88.53 | 16.21 | 19.33 | 18.94 |
| | Speedup (%) | | 81.69 | 78.16 | 78.6 |
| Solid | Time (min) | 0.79 | 0.54 | 0.63 | 0.684 |
| | Speedup (%) | | 31.65 | 20.25 | 13.42 |
| Total | Time (min) | 89.32 | 16.75 | 19.96 | 19.624 |
| | Speedup (%) | | 81.24 | 77.65 | 78.3 |

The case seems to be slightly different for the solid, where in Figures 22 and 23, the displacement and its Fourier's transform at the tip of the flag are shown and seen to reproduce accurately the FOM. The effect of a variation in the stabilization constant for the incompressibility of the fluid is seen in the acceleration and its Fourier transform, shown in Figures 24 and 25 at the tip of the flag. The stabilization constant for the incompressibility affects directly the temporal stability of the solid domain when projected into the ROM space; by restricting further the incompressibility constraint we guarantee a more accurate behavior of the reduced problem. As discussed before, taking a lower stabilization constant fails to reproduce the higher frequency portion of the spectrum (see Figure 25).

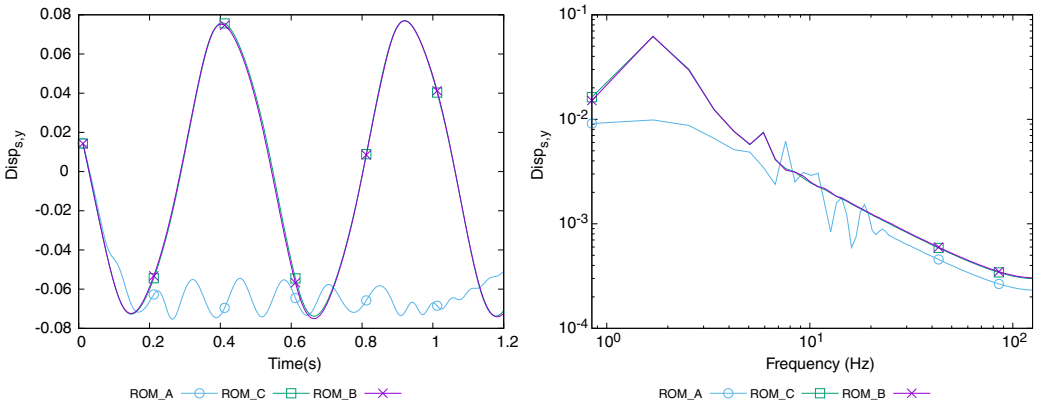


(A) Displacement in $y$ axis (B) Displacement FFT in $y$ axis

**FIGURE 26** Displacement in $y$ and fast Fourier transform at the tip of the flag [Colour figure can be viewed at wileyonlinelibrary.com]

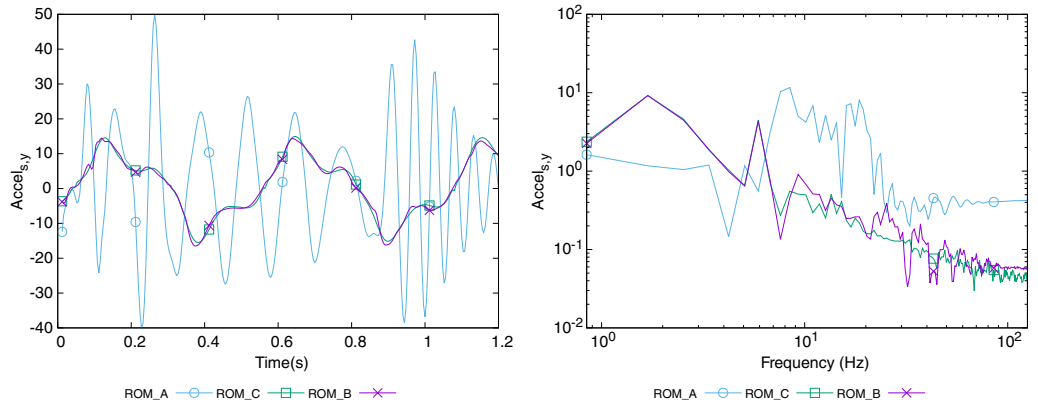


(A) Acceleration in $y$ axis (B) Acceleration FFT in $y$ axis

**FIGURE 27** Acceleration in $y$ and fast Fourier transform at the tip of the flag [Colour figure can be viewed at wileyonlinelibrary.com]

Table 7 shows the total times and speedups for all cases shown. It has to be remarked that we have not used any hyperreduction strategy, and therefore these speedups could be improved. Note that the number of DOF in the fluid for the ROM is just 0.24% of that of the FOM for the richest ROM (163 DOF for the ROM vs 67 926 DOF for the FOM). An ideal implementation would yield a reduction in the computational time solely determined by the number of DOF.

Finally, it is instructive to see the behavior of the FSI-ROM system when not enough basis energy is included into our reduced problem, the next results show a comparison for 99.99% (ROM_A), 99.9999% (ROM_B), and 99.999999% (ROM_C).

Figures 26A and 27B show the evolution of the displacement and acceleration for a point at the tip of beam. While it can be seen that for ROM_B and ROM_C, the solution matches accurately with the results in Reference 49, using less energy (case ROM_A) results in a completely different response, with an over-diffusive displacement (Figure 26A) and amplified modes in the acceleration (Figure 27A). From the Fourier transform of these quantities, it can be seen that failing to reproduce the tail of the spectrum results in an inaccurate approximation of the lower frequencies and spurious high frequencies (see Figures 26B and 27B).

A similar result is seen for the fluid. The pressure evolution at the control point is shown in Figure 28A, where it is observed that the phase and amplitude are completely lost. Regarding the spectrum, Figure 28B shows a completely inaccurate reproduction of the lower energy modes and a diffusive behavior of the lower frequencies.

Overall, it is clear that it is critical to include sufficient energy from both domains, solid and fluid, since otherwise a completely inaccurate solution from the system is obtained.

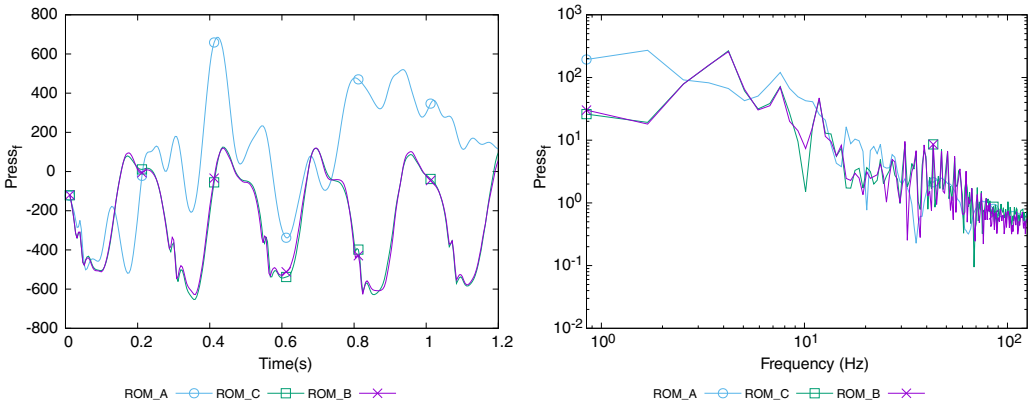


(A) Pressure in $y$ axis

(B) Pressure FFT in $y$ axis

**FIGURE 28** Pressure in $y$ and fast Fourier transform at the tip of the flag [Colour figure can be viewed at wileyonlinelibrary.com]

## 7 | CONCLUSIONS

In this article, we have proposed a ROM model for FSI problems based on the VMS framework. The first conclusion refers to the use of ROM in FSI. In comparison to the work done in Reference 23, where the cases shown could be solved with a basis energy in the range of 80% to 95%, FSI problems seem to be much more sensitive to the amount of energy in the basis necessary to achieve a solution sufficiently close to that of the FOM. It was found that even for the simplest of the cases shown, the problem would not produce any valuable solution with an energy percentage under 99.99% (see Figures 26 to 28). It is possible that this hints to the importance of the high frequencies of the spectrum in the solution of a FSI problem. This remains to be studied further and it is an interesting topic for future work. Nevertheless, in spite of the stringent requirements in terms of retained energy by the ROM, the reduction of the number of DOF with respect to the FOM is still very remarkable.

Once the possibility of reducing drastically the number of DOF has been shown, we have not pursued an efficient implementation of the highly nonlinear problems involved in both the solid and the fluid domains. In particular, we have not implemented any hyperreduction strategy, which should be used on top of the ROM we have proposed. We are currently working on a hyperreduction method based on the existence of a finite element mesh for the ROM.[46]

Partitioned FSI problems have a series of restrictions, such as a maximum time step and the need of diffusive time integration schemes for the ALE framework,[50] that must be met so as to minimize the effect of instabilities like the added mass effect. This in turn is also a restriction on the ROM, making FSI-ROM cases very dependent on how often a snapshot is taken to be able to capture enough of the physics of the problem while keeping instabilities out of the sampling. A richer basis consists of more basis vectors that contain higher frequencies, and in turn, produce a better approximation to the FOM problem. Again, correlating with the above, this hints to the dependency on the high-frequency low-energy modes at the end of the spectrum of the basis.

The VMS-ROM formulation we have proposed for the fluid domain has been found to be accurate and efficient. From the theoretical point of view, it has the interesting feature that the ROM and the FOM problems are solved exactly with the same formulation, only changing the spaces where the unknowns and the test functions belong. From the practical point of view, we have observed that ROM problems with a higher stabilization constant for the incompressibility produced more accurate results that their counterparts with a lower one. We have found convenient to use values of $c_3$ in Equation (10) slightly higher in the ROM than in the FOM.

## ACKNOWLEDGEMENTS

A.T. wants to acknowledge the doctoral scholarship received from the Colombian Government-Colciencias. R.C. acknowledges the support received from the ICREA Acadèmia Research Program of the Catalan Government. J.B. acknowledges the support of the Spanish Government through the Ramón y Cajal grant RYC-2015-17367. This work is partially funded through the ELASTIC-FLOW project, Ref. DPI2015-67857-R of the Spanish Government.

## ORCID

*Alexis Tello* https://orcid.org/0000-0002-5084-1487
*Ramon Codina* https://orcid.org/0000-0002-7412-778X
*Joan Baiges* https://orcid.org/0000-0002-3940-5887


## REFERENCES


1. Richter T. A monolithic geometric multigrid solver for fluid-structure interactions in ALE formulation. *Int J Numer Methods Eng*. 2015;104(5):372-390.
2. Badia S, Nobile F, Vergara C. Fluid-structure partitioned procedures based on Robin transmission conditions. *J Comput Phys*. 2008;227(14):7027-7051.
3. Farhat C, Lakshminarayan VK. An ALE formulation of embedded boundary methods for tracking boundary layers in turbulent fluid-structure interaction problems. *J Comput Phys*. 2014;263:53-70.
4. Farhat C, van der Zee KG, Geuzaine P. Provably second-order time-accurate loosely-coupled solution algorithms for transient nonlinear computational aeroelasticity. *Comput Methods Appl Mech Eng*. 2006;195(17-18):1973-2001.
5. Bordère S, Caltagirone J-P. A unifying model for fluid flow and elastic solid deformation: a novel approach for fluid-structure interaction. *J Fluids Struct*. 2014;51(1):344-353.
6. Yuri Bazilevs VM, Calo YZ, Hughes TJR. Isogeometric fluid-structure interaction analysis with applications to arterial blood flow. *Comput Mech*. 2006;38(4-5):310-322.
7. Bazilevs Y, Calo VM, Hughes TJ, Zhang Y. Isogeometric fluid-structure interaction: theory, algorithms, and computations. *Comput Mech*. 2008;43(1):3-37.
8. Le Tallec P. Fluid structure interaction with large structural displacements. *Comput Methods Appl Mech Eng*. 2001;190(24-25):3039-3067.
9. Baiges J, Codina R, Pont A, Castillo E. An adaptive fixed-mesh ALE method for free surface flows. *Comput Methods Appl Mech Eng*. 2017;159–188(1):313.
10. Glowinski R, Basting S, Quaini A. Extended ALE method for fluid-structure interaction problems with large structural displacements. *J Comput Phys*. 2017;331:312-336.
11. Hou G, Wang J, Layton A. Numerical methods for fluid-structure interaction - a review. *Commun Comput Phys*. 2012;12(2):337-377.
12. Baiges J, Codina R, Idelsohn S. A domain decomposition strategy for reduced order models. application to the incompressible Navier-Stokes equations. *Comput Methods Appl Mech Eng*. 2013;267:23-42.
13. Baiges J, Codina R, Idelsohn S. Explicit reduced-order models for the stabilized finite element approximation of the incompressible Navier-Stokes equations. *Int J Numer Methods Fluids*. 2013;72(12):1219-1243.
14. Schilders W. Introduction to model order reduction. *Model Order Reduction: Theory, Research Aspects and Applications. Mathematics in Industry (The European Consortium for Mathematics in Industry)*. Vol 13. Berlin, Germany / Heidelberg: Springer; 2008:3-32.
15. Sirovich L, Kirby M. Low-dimensional procedure for the characterization of human faces. *J Opt Soc Am A*. 1987;4(3):519-524.
16. Everson R, Sirovich L. Karhunen-Loève procedure for gappy data. *J Opt Soc Am A*. 1995;12(8):1657-1664.
17. Colciago CM, Deparis S. Reduced order models for fluid-structure interaction problems with applications in haemodynamics; 2018. arXiv preprint arXiv: 1801.06127.
18. Ballarin F, Rozza G. POD-Galerkin monolithic reduced order models for parametrized fluid-structure interaction problems. *Int J Numer Methods Fluids*. 2016;82(12):1010-1034.
19. Xiao D, Yang P, Fang F, Xiang J, Pain CC, Navon IM. Non-intrusive reduced order modelling of fluid-structure interactions. *Comput Methods Appl Mech Eng*. 2016;35–54(5):303.
20. Thari A, Pasquariello V, Aage N, Hickel S. Adaptive reduced-order modeling for non-linear fluid-structure interaction; 2017. arXiv preprint arXiv:1702.043321–25, 2 2017.
21. Baiges J, Codina R, Idelsohn S. Reduced-order subscales for POD models. *Comput Methods Appl Mech Eng*. 2015;291(7):173-196.
22. Giere S, Iliescu T, John V, Wells D. SUPG reduced order models for convection-dominated convection-diffusion-reaction equations. *Comput Methods Appl Mech Eng*. 2015;289:454-474.
23. Reyes R, Codina R, Baiges J, Idelsohn S. Reduced order models for thermally coupled low mach flows. *Adv Model Simulat Eng Sci*. 2018;5(1):28.
24. Reyes R, Codina R. Projection-based reduced order models for flow problems: a variational multiscale approach; July 2019
25. Stabile G, Ballarin F, Zuccarino G, Rozza G. A reduced order variational multiscale approach for turbulent flows. *Adv Comput Math*. 2019;45:2349-2368.
26. Fonn E, van Brummelen H, Kvamsdal T, Rasheed A. Fast divergence-conforming reduced basis methods for steady Navier-Stokes flow. *Comput Methods Appl Mech Eng*. 2019;346(4):486-512.
27. Hughes TJ, Feijóo GR, Mazzei L, Quincy JB. The variational multiscale method-a paradigm for computational mechanics. *Comput Methods Appl Mech Eng*. 1998;166(1-2):3-24.
28. Codina R. Stabilization of incompressibility and convection through orthogonal sub-scales in finite element methods. *Comput Methods Appl Mech Eng*. 2000;190(13-14):1579-1599.
29. Codina R. Stabilized finite element approximation of transient incompressible flows using orthogonal subscales. *Comput Methods Appl Mech Eng*. 2002;191(39-40):4295-4321.

30. Codina R, Badia S, Baiges J, Principe J. Variational multiscale methods in computational fluid dynamics. In Stein E, de Borst R; Hughes Thomas J.R. (eds.), *Encyclopedia of Computational Mechanics*. 2nd ed. Hoboken, NJ: John Wiley & Sons; 2018:1-28.
31. Codina R. A stabilized finite element method for generalized stationary incompressible flows. *Comput Methods Appl Mech Eng*. 2001;190(20-21):2681-2706.
32. Belytschko T, Liu WK, Moran B, Elkhodary K. *Nonlinear Finite Elements for Continua and Structures*. 2nd ed. New York: Wiley; 2014:830.
33. Donea J, Huerta A, Ponthot JP, Rodriguez-Ferran A. Arbitrary Lagrangian-Eulerian methods. *Encyclopedia of Computational Mechanics*. Vol 11. Chichester, UK: John Wiley & Sons, Ltd; 2004:1-25.
34. Chiandussi G, Bugeda G, Oñate E. A simple method for automatic update of finite element meshes. *Commun Numer Methods Eng*. 2000;16(1):1-19.
35. Fan J, Liao H, Ke R, et al. A monolithic Lagrangian meshfree scheme for Fluid-structure interaction problems within the OTM framework. *Comput Methods Appl Mech Eng*. 2018;198–219(8):337.
36. Sauer RA, Luginsland T. A monolithic fluid-structure interaction formulation for solid and liquid membranes including free-surface contact. *Comput Methods Appl Mech Eng*. 2018;1–31(11):341.
37. Akbay M, Nobles N, Zordan V, Shinar T. An extended partitioned method for conservative solid-fluid coupling. *ACM Trans Graph*. 2018;37(4):1-12.
38. Langer U, Yang H. Partitioned solution algorithms for fluid-structure interaction problems with hyperelastic models. *J Comput Appl Math*. 2015;47–61(3):276.
39. Förster C, Wall WA, Ramm E. Artificial added mass instabilities in sequential staggered coupling of nonlinear structures and incompressible viscous flows. *Comput Methods Appl Mech Eng*. 2007;196(7):1278-1293.
40. van Brummelen EH. Partitioned iterative solution methods for fluid-structure interaction. *Int J Numer Methods Fluids*. 2011;65(1-3):3-27.
41. Houzeaux G, Codina R. Transmission conditions with constraints in finite element domain decomposition methods for flow problems. *Commun Numer Methods Eng*. 2001;17(3):179-190.
42. Küttler U, Wall WA. Fixed-point fluid-structure interaction solvers with dynamic relaxation. *Comput Mech*. 2008;43(1):61-72.
43. Ballarin F, Manzoni A, Quarteroni A, Rozza G. Supremizer stabilization of POD-Galerkin approximation of parametrized steady incompressible Navier-Stokes equations. *Int J Numer Methods Eng*. 2015;102(5):1136-1161.
44. Carlberg K, Bou-Mosleh C, Farhat C. Efficient non-linear model reduction via a least-squares Petrov-Galerkin projection and compressive tensor approximations. *Int J Numer Methods Eng*. 2011;86(2):155-181.
45. Ryckelynck D. A priori hyperreduction method: an adaptive approach. *J Comput Phys*. 2005;202(1):346-366.
46. Reyes R, Codina R. Element boundary terms in reduced order models for flow problems: domain decomposition and adaptive coarse mesh hyper-reduction; December 2019.
47. Carlberg K, Farhat C, Cortial J, Amsallem D. The GNAT method for nonlinear model reduction: effective implementation and application to computational fluid dynamics and turbulent flows. *J Comput Phys*. 2013;242:623-647.
48. Baiges J. The Fixed-Mesh ALE Method Applied to Multiphysics Problems using Stabilized Formulations (PhD thesis). Universitat Politècnica de Catalunya; 2011.
49. Turek S, Hron J. Proposal for numerical benchmarking of Fluid-structure interaction between an elastic object and laminar incompressible flow. *Fluid-Structure Interaction*. Vol 53. Berlin, Gerkmany / Heidelberg: Springer; 2006:371-385.
50. Forster C. Robust Methods for Fluid-Structure Interaction with Stabilised Finite Elements (PhD thesis). Universitat Stuttgart; 2007.


## SUPPORTING INFORMATION

Additional supporting information may be found online in the Supporting Information section at the end of this article.

**How to cite this article:** Tello A, Codina R, Baiges J. Fluid structure interaction by means of variational multiscale reduced order models. *Int J Numer Methods Eng*. 2020;121:2601–2625. https://doi.org/10.1002/nme.6321